Technische Universität Berlin

Institut für Mechanik
Fachgebiet Kontinuumsmechanik
und Materialtheorie

Analysis and Development of a Monolithic Computational Approach for Fluid–Structure Interaction by means of the Finite Element Method

Masterarbeit

eingereicht von
Florian Piekny, B.Sc.

Gutachter: Prof. Dr. rer. nat. Wolfgang H. Müller
Dr.-Ing. Bilen Emek Abali

Technische Universität Berlin
Fakultät V – Institut für Mechanik
Fachgebiet Kontinuumsmechanik und Materialtheorie
Berlin, 24. September 2019

Eidesstattliche Erklärung

Hiermit erkläre ich, dass ich die vorliegende Arbeit selbständig und eigenhändig sowie ohne unerlaubte fremde Hilfe und ausschließlich unter Verwendung der aufgeführten Quellen und Hilfsmittel angefertigt habe.

Ort, Datum	Florian Piekny, B.Sc.

Acknowledgements

I want to express my gratitude to Dr. Bilen Emek Abali for everything I was allowed to learn from him—especially within the scope of our collaboration for this thesis but also during his lectures on *Computational Reality*. Further, I thank him for the provision of the necessary computational resources for the realization of this work.

Abstract

The phenomenon of fluid–structure interaction (FSI) appears in many engineering applications. Its computation allows to quantify the mechanical behaviour of both fluid and structure interacting with each other. For that purpose, appropriate field equations are specified for an incompressible, viscous fluid and a linear elastic solid. The domain movement is considered by utilizing the *arbitrary LAGRANGEan–EULERian* viewpoint for the fluid equations. Within a monolithic computational approach the fluid and structure equations are solved numerically in the reference configuration by means of the finite element method (FEM). The solution method is validated using numerically computed reference data for a benchmark problem. A novel FEM is introduced for the monolithic computation of FSI allowing a straightforward coupling to further field quantities. It is then extended to a computational approach for the thermomechanical FSI of an incompressible NAVIER–STOKES–FOURIER fluid and a linear thermoelastic structure.

Zusammenfassung

Das Phänomen der Fluid–Struktur–Interaktion (FSI) tritt in zahlreichen technischen Systemen auf. Die Berechnung der FSI ermöglicht eine Quantifizierung des mechanischen Verhaltens der miteinander interagierenden Fluide und Strukturen. Dafür werden die entsprechenden Feldgleichungen für ein inkompressibles, viskoses Fluid und eine linear-elastische Struktur bestimmt. Die Bewegung des Definitionsbereichs wird durch die Verwendung der *arbitrary* *LAGRANGEan–EULERian* Betrachtungsweise für die Fluidgleichungen berücksichtigt. Innerhalb eines monolithischen Berechnungsansatzes werden die Fluid- und Strukturgleichungen in der Referenzkonfiguration numerisch mithilfe der Finite–Elemente–Methode (FEM) gelöst. Die Lösungsmethode wird mit numerisch ermittelten Daten für ein Vergleichsproblem validiert. Eine neuartige FEM für die monolithische Berechnung der FSI, welche eine einfache Kopplung zu weiteren Feldgrößen ermöglicht, wird eingeführt. Diese wird anschließend zu einem Berechnungsansatz für die thermomechanische FSI eines inkompressiblen NAVIER–STOKES–FOURIER–Fluids und einer linear-thermoelastischen Struktur erweitert.

Contents

List of Symbols

Latin symbol	*Description*	*SI units*
c	Specific heat capacity	J/(kg K)
C_{ijkl}	Stiffness tensor	Pa
d_i	Mesh displacement	m
$\mathrm{d}a$	Area element in spatial coordinates	m^2
$\mathrm{d}A$	Area element in material coordinates	m^2
$\mathrm{d}\hat{A}$	Area element in referential coordinates	m^2
$\mathrm{d}v$	Volume element in spatial coordinates	m^3
$\mathrm{d}V$	Volume element in material coordinates	m^3
$\mathrm{d}\hat{V}$	Volume element in referential coordinates	m^3
E_{ij}	Green–Lagrange strain	1
f_i	Specific volumetric force	N/kg
F_{ij}	Deformation gradient	1
$\hat{F}_{ij}$	Mesh deformation gradient	1
J	Determinant of deformation gradient	1
$\hat{J}$	Determinant of mesh deformation gradient	1
n_i	Plane normal in spatial coordinates	1
N_i	Plane normal in material coordinates	1
$\hat{N}_i$	Plane normal in referential coordinates	1
p	Pressure	Pa
$\bar{p}$	Artificial pressure	Pa
P_{ij}	Nominal stress	Pa
q	Heat flux in normal direction	$\mathrm{W/m}^2$
q_i	Heat flux in spatial coordinates	$\mathrm{W/m}^2$
Q_i	Heat flux in material coordinates	$\mathrm{W/m}^2$
r	Internal heating	W/kg
S_{ij}	Second Piola–Kirchhoff stress	Pa
t	Time	s
t_i	Traction	Pa
T	Temperature	K
u	Specific internal energy	J/kg
u_i	Displacement	m
v_i	Velocity	m/s
w_i	Mesh velocity	m/s

x_i	Spatial coordinates in a Cartesian system	m
X_i	Material coordinates in a Cartesian system	m

Greek symbol	*Description*	*SI units*
α^{disp}	Mesh motion coefficient	$\text{N}/(\text{m}^2\text{s})$
α^{pres}	Artificial pressure coefficient	$\text{m}^3\text{s}/\text{kg}$
α_{ij}, α	Coefficient of thermal expansion	1/K
Γ	Boundary of a volume	m^2
δ_{ij}	KRONECKER symbol	1
δp	Test function for pressure	Pa
δv_i	Test function for velocity	m/s
δu_i	Test function for displacement	m
η	Specific entropy	J/(K kg)
κ	Thermal conductivity	W/(m K)
λ	LAMÉ's first parameter	Pa
μ^{F}	Dynamic viscosity	$\text{N s}/\text{m}^2$
μ^{S}	LAMÉ's second parameter	Pa
ρ	Mass density	kg/m^3
ρ_0	Initial mass density	kg/m^3
σ_{ij}	CAUCHY stress	Pa
φ_i	Material motion	m
Φ_i	Mesh motion	m
χ_i	Mesh coordinates in a Cartesian system	m
Ω	Volume	m^3

1 Introduction

Whenever fluid and solid exert forces on each other that affect their motions, the phenomenon of fluid–structure interaction (FSI) is present. The term FSI is primarily used to describe such a mechanical interaction between fluid and structure.

The following two sections explain the motivation for the consideration of FSI and introduce the problem formulation of this thesis.

1.1 Motivation

FSI appears in many engineering applications. A typical example can be observed at flying aircrafts. Due to the coupling of structural dynamics and areodynamics, the airfoils undergo relatively large deflections and oscillations as shown in Fig. 1.1. In order to prevent a failure because of these deflections,

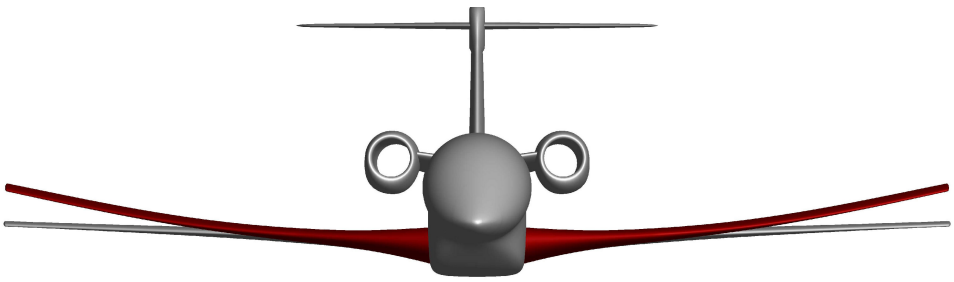

Fig. 1.1: Illustration of airfoil deflection due to FSI (Piaggio P1XX, [7])

we need to study FSI. Other prominent examples of FSI can be also found in the field of aerodynamics—like the interaction of air flow with wind turbines or buildings. The collapse of the *Tacoma Narrows Bridge* (1940) represents an unfortunate example of the latter one. Further applications reach from the wide field of turbo machinery (gas turbines, turbo chargers, gas foil bearings) to hydrodynamics (ship propellers, ship hulls, pumps, tank walls) and hemodynamics (blood vessels, heart valves). These examples represent only a fractional amount of the possible areas of application for FSI. Depending on the aforementioned applications, the consideration of FSI can be vital for

medical purposes and for the efficiency, dependability and durability of highly sophisticated products.

1.2 Problem formulation and objectives of this work

FSI can be quantified experimentally or numerically. As experiments are usually very expensive and sometimes even impossible to realize, a lot of effort has been invested in the past decades in order to develop numerical methods that allow a simulation of FSI.

As discretization scheme for the governing partial differential equations (PDEs), the finite volume method (FVM) and the finite element method (FEM) are often utilized. The latter is employed in this thesis. Furthermore, we restrict ourselves to incompressible fluids. This assumption is still justified for a lot of applications, especially, in hydro- and hemodynamics.

Basically, there exist two solution strategies: *partitioned* and *monolithic* approaches. Partitioned methods ([20], [2, p. 99]) treat the fluid and structure problems separately, i.e., with different solvers. The interaction is realized via exchange of interface/boundary conditions. Since the problems are solved sequentially, several subiterations are necessary to reach convergence of the fluid and structure subproblems. For instance, a subiteration could be the following procedure:

1. Solve the structure problem for the velocity of the structure with the given stress caused by the fluid as boundary condition on the interface.

2. Solve the fluid problem, especially, for the stress on the interface with the given velocity caused by the structure as boundary condition on the interface.

3. If convergence is reached, exit the subiteration, otherwise go to 1.

According to [6] this procedure is also called a staggered algorithm. The biggest benefit of the partitioned approach is that existing iterative solvers for fluid and structural dynamics, respectively, can be used. However, a lack of convergence is reported for a number of problems [6]. This applies to problems in which an incompressible fluid is fully contained by a structure [19]. Moreover, problems in which the densities of the fluid and the structure are of the same order cause poor convergence behaviour [35, p. 41]. This pertains in particular to biomedical applications.

In monolithic methods, the fluid and structure subproblems are combined into one problem. Thus, the fluid and structure equations are solved simultaneously with a single solver and a common discretization technique for spatial and temporal discretization. The interface conditions, i.e., the continuity of

velocities and the equilibrium of forces are satisfied by definition of the monolithic problem such that no subiterations are needed for the fulfillment of the interaction conditions. That is why monolithic methods are also referred to as strongly coupled algorithms [6]. The main advantage is that, in general, monolithic approaches seem to be more robust than partitioned algorithms [6, 23]. However, iterative solvers for fluid and structural dynamics cannot be used without further modifications [35, p. 91].

The first objective of this thesis is to develop a monolithic computational approach for FSI using the open-source packages of the FEniCS project [3]. Before, the necessary fundamentals have to be studied. The developed algorithm is then supposed to be validated by comparing its results to numerically computed reference data of a benchmark setting described in [31]. Alternative methods within a monolithic approach shall be discussed and examined. Particularly, the method introduced in [1] is employed for the computation of the fluid flow. Additionally, an extension to thermomechanical FSI by means of the monolithic approach is intended such that the coupled thermal and mechanical FSI problem can be solved simultaneously.

2 Continuum mechanical fundamentals

In this chapter some fundamentals of continuum mechanics are presented. First, different kinematical descriptions and coordinate transformations are introduced. Further, the necessary balance equations and constitutive relations are presented. Throughout the work we make use of EINSTEIN's summation convention.

2.1 Kinematical descriptions and coordinate transformations

When dealing with FSI the choice of proper kinematical description for both fluid and solid domain is required. To illustrate the different kinematical descriptions or viewpoints, consider the example of a channel filled with a certain amount of fluid (blue) in Fig. 2.1. At the time $t = t_0$ the fluid is situated

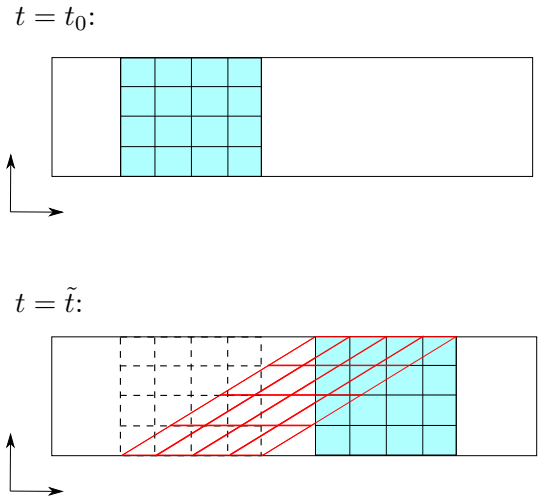

Fig. 2.1: Illustration of LAGRANGEan, EULERian and ALE viewpoints

at the left side of the channel segment. Since the fluid quantities are of interest, let a domain, which is shown as a grid (also called mesh), be defined where the fluid is located. Now, the governing equations for the fluid flow, nonlinear

partial differential equations (PDEs), have to be fulfilled in that domain and, particularly, in the vertices or nodes of the domain in order to compute, e.g., the mass density of the fluid. At the next time instant, at time $t = \tilde{t}$, the fluid particles have moved to the right. Depending on the movement of the domain at $t = \tilde{t}$, there exist the following three viewpoints:

- The LAGRANGEan viewpoint: All mesh nodes, i.e., the whole domain moves with the fluid particles.
- The EULERian viewpoint: The domain (shown dashed) does not move at all and remains at its original position.
- The *arbitrary LAGRANGEan–EULERian* (ALE) viewpoint: The domain (red) moves completely arbitrarily. Moreover, it is possible that some nodes move with the material (here the upper nodes) while other nodes do not change their position (lower nodes).

Note that each of the three domains at time $t = \tilde{t}$ is described in a coordinate system which is fixed in space and time. Therefore, the respective domain is called spatial domain, Ω^x, and described by spatial coordinates, x_i.

In the literature, the introduced viewpoints are sometimes named LAGRANGEan/EULERian/ALE *observer*. This wording is misleading as one identifies an observer with a coordinate system in which physical quantities are expressed. In this work the observer can be visualized by the spatial Cartesian system in Fig. 2.1.

The moving spatial domain Ω^x of the LAGRANGEan viewpoint can be transformed from the current configuration to a reference configuration, which can be chosen as the set of fluid particles at time $t = t_0$ (see Fig. 2.2). The

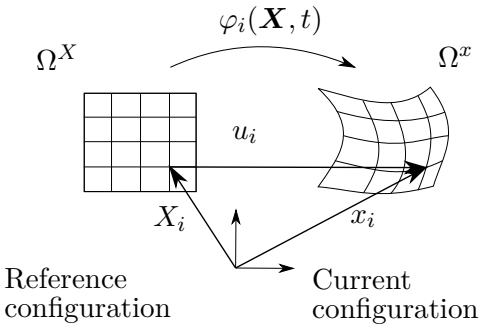

Fig. 2.2: LAGRANGEan description of motion

domain in the reference configuration is then termed material domain, Ω^X, and described by material coordinates, X_i, which physically denote the massive particles in the continuum body. The displacement is denoted by u_i and the

motion of the continuum by $\varphi_i(\boldsymbol{X}, t)$ such that[1]

$$x_i = \varphi_i(\boldsymbol{X}, t) = X_i + u_i. \tag{2.1}$$

The deformation of the continuum is characterized by the deformation gradient, F_{ij},

$$F_{ij} = \frac{\partial x_i}{\partial X_j} = \delta_{ij} + \frac{\partial u_i}{\partial X_j} \qquad \text{with} \quad J = \det\left(\frac{\partial x_i}{\partial X_j}\right), \tag{2.2}$$

and its inverse,

$$\left(\boldsymbol{F}^{-1}\right)_{ij} = \frac{\partial X_i}{\partial x_j} = \delta_{ij} - \frac{\partial u_i}{\partial x_j}. \tag{2.3}$$

In an analogous manner the moving spatial domain Ω^x of the ALE viewpoint can be transformed from the current configuration to a reference configuration, which can be chosen as the set of mesh nodes at time $t = t_0$ (see Fig. 2.3). The

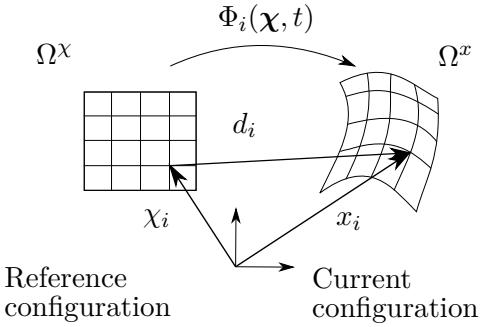

Fig. 2.3: ALE description of motion

domain in the reference configuration is then termed referential domain, Ω^χ, and described by referential coordinates, χ_i, whereas these coordinates fail to have a physical meaning. The mesh displacement is denoted by d_i and the motion of the mesh by $\Phi_i(\boldsymbol{\chi}, t)$ such that

$$x_i = \Phi_i(\boldsymbol{\chi}, t) = \chi_i + d_i. \tag{2.4}$$

The deformation of the mesh is characterized by the mesh deformation gradient, $\hat{F}_{ij}$,

$$\hat{F}_{ij} = \frac{\partial x_i}{\partial \chi_j} = \delta_{ij} + \frac{\partial d_i}{\partial \chi_j} \qquad \text{with} \quad \hat{J} = \det\left(\frac{\partial x_i}{\partial \chi_j}\right), \tag{2.5}$$

[1] For reasons of clarity function arguments are only used in this thesis when regarded as necessary for comprehension by the author. The displacement, u_i, is of course also a function of X_i and t.

and its inverse,

$$\left(\hat{\boldsymbol{F}}^{-1}\right)_{ij} = \frac{\partial \chi_i}{\partial x_j} = \delta_{ij} - \frac{\partial d_i}{\partial x_j}. \tag{2.6}$$

Note that the material and referential domains do not necessarily have to coincide geometrically as in Fig. 2.2 and Fig. 2.3, but yet they often do. Furthermore, the current and the reference configuration for the EULERian viewpoint are identical.

Once a viewpoint is determined, the PDE can be formulated in the corresponding current or reference configuration, i.e., in spatial, material or referential coordinates. According to [11, p. 417] and [34, p. 12] a physical quantity can be described in each of the introduced domains:

$$f^{***}(\boldsymbol{X}, t) = f^{**}(\boldsymbol{\chi}, t) = f^{*}(\boldsymbol{x}, t). \tag{2.7}$$

The employed stars shall indicate that the functional forms are, in general, different. The material and the spatial description of the physical quantity can be related by the motion of the continuum defined in Eq. (2.1) such that

$$f^{***}(\boldsymbol{X}, t) = f^{*}(\boldsymbol{\varphi}(\boldsymbol{X}, t), t). \tag{2.8}$$

Analogously, the referential and the spatial description of the physical quantity are connected via the mesh motion defined in Eq. (2.4) such that

$$f^{**}(\boldsymbol{\chi}, t) = f^{*}(\boldsymbol{\Phi}(\boldsymbol{\chi}, t), t). \tag{2.9}$$

Consequently, spatial derivatives can be transformed by use of the chain rule:

$$\frac{\partial f^{***}}{\partial X_i} = \frac{\partial f^{*}}{\partial x_j}\frac{\partial x_j}{\partial X_i} = \frac{\partial f^{*}}{\partial x_j} F_{ji} \Leftrightarrow \frac{\partial f^{*}}{\partial x_i} = \frac{\partial f^{***}}{\partial X_j}\frac{\partial X_j}{\partial x_i} = \frac{\partial f^{***}}{\partial X_j}\left(\boldsymbol{F}^{-1}\right)_{ji}, \tag{2.10}$$

$$\frac{\partial f^{**}}{\partial \chi_i} = \frac{\partial f^{*}}{\partial x_j}\frac{\partial x_j}{\partial \chi_i} = \frac{\partial f^{*}}{\partial x_j} \hat{F}_{ji} \Leftrightarrow \frac{\partial f^{*}}{\partial x_i} = \frac{\partial f^{**}}{\partial \chi_j}\frac{\partial \chi_j}{\partial x_i} = \frac{\partial f^{**}}{\partial \chi_j}\left(\hat{\boldsymbol{F}}^{-1}\right)_{ji}. \tag{2.11}$$

For the transformation of a volume element $\mathrm{d}v$ in spatial coordinates follows that [2, p. 21]

$$\mathrm{d}v = J\,\mathrm{d}V \Rightarrow \mathrm{d}v = \hat{J}\,\mathrm{d}\hat{V}, \tag{2.12}$$

where $\mathrm{d}V$ and $\mathrm{d}\hat{V}$ are the respective volume elements in material and referential coordinates. The corresponding area elements are related via

$$n_j\,\mathrm{d}a = J\left(\boldsymbol{F}^{-1}\right)_{kj} N_k\,\mathrm{d}A \tag{2.13}$$

$$\Rightarrow n_j\,\mathrm{d}a = \hat{J}\left(\hat{\boldsymbol{F}}^{-1}\right)_{kj} \hat{N}_k\,\mathrm{d}\hat{A}, \tag{2.14}$$

with the area elements $\mathrm{d}a$, $\mathrm{d}A$, $\mathrm{d}\hat{A}$ and the plane normals n_j, N_j, $\hat{N}_j$ expressed in spatial, material and referential coordinates, respectively.

Regardless of the utilized coordinates the selected viewpoint always implies a certain interpretation of the time derivatives in the considered PDE which takes into account the movement of the domain. Corresponding to the kinematical descriptions the following kinds of time derivatives are introduced:

- material time derivative, $\frac{\partial(\cdot)}{\partial t}|_{\boldsymbol{X}}$, for the LAGRANGEan viewpoint,
- spatial time derivative, $\frac{\partial(\cdot)}{\partial t}|_{\boldsymbol{x}}$, for the EULERian viewpoint,
- referential time derivative, $\frac{\partial(\cdot)}{\partial t}|_{\boldsymbol{\chi}}$, for the ALE viewpoint.

Here the vertical bar means that the respective coordinate, i.e., a material particle, X_i, a spatial point, x_i, or a mesh node, χ_i, is held constant. The material time derivative of a physical quantity can be related to its spatial time derivative by use of the chain rule, Eq. (2.8) and the fact that material coordinates are constant in time:

$$\begin{aligned} \frac{\mathrm{d}f^{***}(\boldsymbol{X},t)}{\mathrm{d}t} &= \frac{\mathrm{d}f^{*}(\boldsymbol{\varphi}(\boldsymbol{X},t),t)}{\mathrm{d}t} \\ \Leftrightarrow \frac{\partial f^{***}}{\partial t} &= \frac{\partial f^{*}}{\partial t} + \frac{\partial f^{*}}{\partial x_i}\frac{\partial \varphi_i(\boldsymbol{X},t)}{\partial t} \\ \Leftrightarrow \frac{\partial f^{***}}{\partial t} &= \frac{\partial f^{*}}{\partial t} + v_i\frac{\partial f^{*}}{\partial x_i}. \end{aligned} \tag{2.15}$$

Dropping the notation with stars Eq. (2.15) can be expressed by

$$\left.\frac{\partial f}{\partial t}\right|_{\boldsymbol{X}} = \left.\frac{\partial f}{\partial t}\right|_{\boldsymbol{x}} + v_i\frac{\partial f}{\partial x_i}. \tag{2.16}$$

In the latter two equations the velocity of a material particle, v_i, is defined as the partial time derivative of the particle motion:

$$v_i = \frac{\partial \varphi_i(\boldsymbol{X},t)}{\partial t} = \left.\frac{\partial \varphi_i}{\partial t}\right|_{\boldsymbol{X}} = \frac{\partial u_i}{\partial t}. \tag{2.17}$$

Similarly, the referential time derivative of a physical quantity can be related to its spatial time derivative by evaluating Eq. (2.9):

$$\begin{aligned} \frac{\mathrm{d}f^{**}(\boldsymbol{\chi},t)}{\mathrm{d}t} &= \frac{\mathrm{d}f^{*}(\boldsymbol{\Phi}(\boldsymbol{\chi},t),t)}{\mathrm{d}t} \\ \Leftrightarrow \frac{\partial f^{**}}{\partial t} &= \frac{\partial f^{*}}{\partial t} + \frac{\partial f^{*}}{\partial x_i}\frac{\partial \Phi_i(\boldsymbol{\chi},t)}{\partial t} \\ \Leftrightarrow \frac{\partial f^{**}}{\partial t} &= \frac{\partial f^{*}}{\partial t} + w_i\frac{\partial f^{*}}{\partial x_i}, \end{aligned} \tag{2.18}$$

which is equivalent to

$$\left.\frac{\partial f}{\partial t}\right|_{\boldsymbol{\chi}} = \left.\frac{\partial f}{\partial t}\right|_{\boldsymbol{x}} + w_i \frac{\partial f}{\partial x_i}. \tag{2.19}$$

The mesh velocity, w_i, is introduced as the partial time derivative of the mesh motion:

$$w_i = \frac{\partial \Phi_i(\boldsymbol{\chi}, t)}{\partial t} = \left.\frac{\partial \Phi_i}{\partial t}\right|_{\boldsymbol{\chi}} = \frac{\partial d_i}{\partial t}. \tag{2.20}$$

Both Eq. (2.16) and Eq. (2.19) consitute vital relations between the viewpoints making it possible to switch between different viewpoints.

Remark. *The concepts of kinematical viewpoints and coordinates differ fundamentally. For example, choosing a* LAGRANGEan *kinematical description implies using material time derivatives for all time derivatives in the considered PDE. We stress that this choice does not necessarily lead to a material domain—a material domain is described by material coordinates which are sometimes even called* LAGRANGEan *coordinates in the literature. Rather the choice of coordinates is arbitrary since by Eq.* (2.8) *we have*

$$\left.\frac{\partial f}{\partial t}\right|_{\boldsymbol{X}} = \frac{\partial f^{***}(\boldsymbol{X}, t)}{\partial t} = \left.\frac{\partial f^{*}(\boldsymbol{\varphi}(\boldsymbol{X}, t), t)}{\partial t}\right|_{\boldsymbol{X}}. \tag{2.21}$$

The same argumentation holds for the ALE viewpoint:

$$\left.\frac{\partial f}{\partial t}\right|_{\boldsymbol{\chi}} = \frac{\partial f^{**}(\boldsymbol{\chi}, t)}{\partial t} = \left.\frac{\partial f^{*}(\boldsymbol{\Phi}(\boldsymbol{\chi}, t), t)}{\partial t}\right|_{\boldsymbol{\chi}}. \tag{2.22}$$

2.2 Balance equations

In this section the balances of mass, linear momentum and internal energy are introduced.

The balances of mass and linear momentum form an essential part of the field equations that have to be solved for FSI problems, which usually constitute purely mechanical and thus isothermal problems.

The additional consideration of the balance of internal energy allows to formulate thermomechanical FSI problems. Moreover, the balance of internal energy is rewritten by using GIBBS's equation such that we obtain the balance of entropy.

The introduced balance equations are motivated in [2] and presented in their well-known EULERian and LAGRANGEan local forms.

2.2.1 EULERian form

The balance equations in EULERian form imply the EULERian viewpoint and are formulated in spatial coordinates. The balance of mass reads [2, p. 77]

$$\left.\frac{\partial \rho}{\partial t}\right|_{\boldsymbol{x}} + \frac{\partial \rho v_i}{\partial x_i} = 0, \tag{2.23}$$

and the balance of linear momentum is given by [2, p. 77]

$$\left.\frac{\partial \rho v_i}{\partial t}\right|_{\boldsymbol{x}} + \frac{\partial \rho v_j v_i}{\partial x_j} - \frac{\partial \sigma_{ji}}{\partial x_j} - \rho f_i = 0, \tag{2.24}$$

where ρ is the mass density, σ_{ji} the CAUCHY stress, and f_i the specific volumetric force. The balance equations are typically utilized in this form to describe fluid dynamics.

The balance of internal energy reads [2, p. 113]

$$\rho \dot{u} + \frac{\partial q_i}{\partial x_i} - \rho r = \sigma_{ij} \frac{\partial v_j}{\partial x_i}, \tag{2.25}$$

where $\dot{u}$ denotes the material time derivative of the specific internal energy, u:

$$\dot{u} = \left.\frac{\partial u}{\partial t}\right|_{\boldsymbol{X}} = \left.\frac{\partial u}{\partial t}\right|_{\boldsymbol{x}} + v_i \frac{\partial u}{\partial x_i}. \tag{2.26}$$

The heat flux in spatial coordinates is given by q_i and the internal heating by r.

For the derivation of the balance of entropy, we split the following quantities into a reversible and a dissipative part:

$$u = {}^{\mathrm{r}}u + {}^{\mathrm{d}}u, \qquad \sigma_{ij} = {}^{\mathrm{r}}\sigma_{ij} + {}^{\mathrm{d}}\sigma_{ij}, \qquad \frac{\partial q_i}{\partial x_i} = {}^{\mathrm{r}}\left(\frac{\partial q_i}{\partial x_i}\right) + {}^{\mathrm{d}}\left(\frac{\partial q_i}{\partial x_i}\right). \tag{2.27}$$

Further, we assume that the internal energy is reversible, i.e. ${}^{\mathrm{d}}u = 0$, and introduce the specific entropy, η, by ([2, p. 128], [9])

$${}^{\mathrm{r}}\left(\frac{\partial q_i}{\partial x_i}\right) = -T\rho\dot{\eta}, \tag{2.28}$$

where T denotes the temperature. The formulation of the balance of internal energy given in Eq. (2.25) at thermal and mechanical equilibrium then leads to an alternative form of GIBBS's equation which is also known as the fundamental

thermodynamic relation[2]:

$$\rho\dot{u} - T\rho\dot{\eta} = {}^{\mathrm{r}}\sigma_{ij}\frac{\partial v_j}{\partial x_i}. \tag{2.29}$$

The internal heating term has to vanish at equilibrium and does, therefore, not appear in Eq. (2.29). Next, we insert the GIBBS's equation into the balance of internal energy in Eq. (2.25) and bring it into the EULERian form of the balance of entropy:

$$\begin{aligned}
T\rho\dot{\eta} + {}^{\mathrm{r}}\sigma_{ij}\frac{\partial v_j}{\partial x_i} + \frac{\partial q_i}{\partial x_i} - \rho r &= \left({}^{\mathrm{r}}\sigma_{ij} + {}^{\mathrm{d}}\sigma_{ij}\right)\frac{\partial v_j}{\partial x_i} \\
\Leftrightarrow T\rho\dot{\eta} + \frac{\partial q_i}{\partial x_i} - \rho r &= {}^{\mathrm{d}}\sigma_{ij}\frac{\partial v_j}{\partial x_i} \\
\Leftrightarrow \rho\dot{\eta} + \frac{1}{T}\frac{\partial q_i}{\partial x_i} - \rho\frac{r}{T} &= \frac{1}{T}\,{}^{\mathrm{d}}\sigma_{ij}\frac{\partial v_j}{\partial x_i} \\
\Leftrightarrow \rho\dot{\eta} + \frac{\partial}{\partial x_i}\left(\frac{q_i}{T}\right) - q_i\frac{\partial}{\partial x_i}\left(\frac{1}{T}\right) - \rho\frac{r}{T} &= \frac{1}{T}\,{}^{\mathrm{d}}\sigma_{ij}\frac{\partial v_j}{\partial x_i} \\
\Leftrightarrow \rho\dot{\eta} + \frac{\partial}{\partial x_i}\left(\frac{q_i}{T}\right) - \rho\frac{r}{T} &= \frac{1}{T}\,{}^{\mathrm{d}}\sigma_{ij}\frac{\partial v_j}{\partial x_i} - \frac{q_i}{T^2}\frac{\partial T}{\partial x_i} \\
\Leftrightarrow \rho\left(\left.\frac{\partial\eta}{\partial t}\right|_{\boldsymbol{x}} + v_i\frac{\partial\eta}{\partial x_i}\right) + \frac{\partial}{\partial x_i}\left(\frac{q_i}{T}\right) - \rho\frac{r}{T} &= \frac{1}{T}\,{}^{\mathrm{d}}\sigma_{ij}\frac{\partial v_j}{\partial x_i} - \frac{q_i}{T^2}\frac{\partial T}{\partial x_i}.
\end{aligned} \tag{2.30}$$

The right-hand side of Eq. (2.30) constitutes the entropy production which has to be positive according to the second law of thermodynamics [13].

2.2.2 LAGRANGEan form

In the LAGRANGEan form, the balance equations imply the LAGRANGEan viewpoint and are formulated in material coordinates. The balance of mass becomes [2, p. 22]

$$\rho_0 = J\rho, \tag{2.31}$$

and the balance of linear momentum reads [2, p. 22]

$$\rho_0\left.\frac{\partial v_i}{\partial t}\right|_{\boldsymbol{X}} - \frac{\partial P_{ki}}{\partial X_k} - \rho_0 f_i = 0, \tag{2.32}$$

where ρ_0 is the initial mass density and P_{ki} the nominal stress defined by

$$P_{ki} = \left(\boldsymbol{F}^{-1}\right)_{kj}\sigma_{ji}J. \tag{2.33}$$

[2] The derivation of GIBBS's equation in its original form is shown in [2, p. 129] for a fluid without elasticity such that ${}^{\mathrm{r}}\sigma_{ij} = -p\delta_{ij}$.

In this form the balance equations are often used in solid mechanics.

The balance of internal energy is given by [2, p. 143]

$$\rho_0 \dot{u} + \frac{\partial Q_i}{\partial X_i} - \rho_0 r = S_{ij} \dot{E}_{ij}, \tag{2.34}$$

with the second PIOLA–KIRCHHOFF stress, S_{ij}, the GREEN–LAGRANGE strain, E_{ij}, and the heat flux in material coordinates, Q_i, [2, p. 142]

$$Q_i^{\mathrm{S}} = q_j^{\mathrm{S}} \left(\boldsymbol{F}^{-1} \right)_{ij} J. \tag{2.35}$$

For the derivation of the balance of entropy, we split the following quantities into a reversible and a dissipative part:

$$u = {}^{\mathrm{r}}u + {}^{\mathrm{d}}u, \qquad S_{ij} = {}^{\mathrm{r}}S_{ij} + {}^{\mathrm{d}}S_{ij}, \qquad \frac{\partial Q_i}{\partial X_i} = {}^{\mathrm{r}}\left(\frac{\partial Q_i}{\partial X_i} \right) + {}^{\mathrm{d}}\left(\frac{\partial Q_i}{\partial X_i} \right). \tag{2.36}$$

As in the previous subsection, we assume that the internal energy is reversible, i.e. ${}^{\mathrm{d}}u = 0$, and analogously introduce the specific entropy by

$${}^{\mathrm{r}}\left(\frac{\partial Q_i}{\partial X_i} \right) = -T \rho_0 \dot{\eta}. \tag{2.37}$$

This leads to the following GIBBS's equation:

$$\rho_0 \dot{u} - T \rho_0 \dot{\eta} = {}^{\mathrm{r}}S_{ij} \dot{E}_{ij}. \tag{2.38}$$

Hereafter, we insert the GIBBS's equation into the balance of internal energy in Eq. (2.34) and rewrite it as the balance of entropy in LAGRANGEan form:

$$\begin{aligned}
T \rho_0 \dot{\eta} + {}^{\mathrm{r}}S_{ij} \dot{E}_{ij} + \frac{\partial Q_i}{\partial X_i} - \rho_0 r &= \left({}^{\mathrm{r}}S_{ij} + {}^{\mathrm{d}}S_{ij} \right) \dot{E}_{ij} \\
\Leftrightarrow T \rho_0 \dot{\eta} + \frac{\partial Q_i}{\partial X_i} - \rho_0 r &= {}^{\mathrm{d}}S_{ij} \dot{E}_{ij} \\
\Leftrightarrow \rho_0 \dot{\eta} + \frac{1}{T} \frac{\partial Q_i}{\partial X_i} - \rho_0 \frac{r}{T} &= \frac{1}{T} \, {}^{\mathrm{d}}S_{ij} \dot{E}_{ij} \\
\Leftrightarrow \rho_0 \dot{\eta} + \frac{\partial}{\partial X_i} \left(\frac{Q_i}{T} \right) - Q_i \frac{\partial}{\partial X_i} \left(\frac{1}{T} \right) - \rho_0 \frac{r}{T} &= \frac{1}{T} \, {}^{\mathrm{d}}S_{ij} \dot{E}_{ij} \\
\Leftrightarrow \rho_0 \dot{\eta} + \frac{\partial}{\partial X_i} \left(\frac{Q_i}{T} \right) - \rho_0 \frac{r}{T} &= \frac{1}{T} \, {}^{\mathrm{d}}S_{ij} \dot{E}_{ij} - \frac{Q_i}{T^2} \frac{\partial T}{\partial X_i} \\
\Leftrightarrow \rho_0 \left. \frac{\partial \eta}{\partial t} \right|_{\boldsymbol{X}} + \frac{\partial}{\partial X_i} \left(\frac{Q_i}{T} \right) - \rho_0 \frac{r}{T} &= \frac{1}{T} \, {}^{\mathrm{d}}S_{ij} \left. \frac{\partial E_{ij}}{\partial t} \right|_{\boldsymbol{X}} - \frac{Q_i}{T^2} \frac{\partial T}{\partial X_i}.
\end{aligned} \tag{2.39}$$

2.3 Constitutive equations

In order to close the system of equations, constitutive equations are required. By these equations the behaviour of the respective material is considered.

2.3.1 Viscous fluid

The simplest constitutive equation for a viscous fluid is the so called NAVIER–STOKES's equation [2, p. 79],

$$\sigma_{ji} = -p\delta_{ji} + \lambda \frac{\partial v_k}{\partial x_k}\delta_{ji} + \mu^{\mathrm{F}} \left(\frac{\partial v_j}{\partial x_i} + \frac{\partial v_i}{\partial x_j} \right), \tag{2.40}$$

where p denotes the pressure, δ_{ji} the KRONECKER symbol, μ^{F} the dynamic viscosity and λ the LAMÉ's first parameter. This constitutive equation connects the CAUCHY stress with the velocity and the pressure which are often solved for fluids.

2.3.2 Linear elastic solid

For an isotropic and linear elastic solid the ST. VENANT–KIRCHHOFF constitutive relation is [2, p. 23]

$$S_{kj} = \lambda E_{ll}\delta_{kj} + 2\mu^{\mathrm{S}} E_{kj}, \tag{2.41}$$

introducing the LAMÉ's second parameter μ^{S}. The second PIOLA–KIRCHHOFF stress is related to the nominal stress by

$$P_{ki} = F_{ij} S_{kj}, \tag{2.42}$$

while for the GREEN–LAGRANGE strain holds

$$E_{kj} = \frac{1}{2} \left(F_{ik} F_{ij} - \delta_{kj} \right). \tag{2.43}$$

The deformation gradient F_{ij} defined in Eq. (2.2) contains the displacement of the continuum and, thus, Eq. (2.41)-Eq. (2.43) describe a relation between the nominal stress, P_{ki}, and the displacement, u_i, which is usually solved for the solid.

2.3.3 Navier–Stokes–Fourier fluid

A viscous and thermally conductive fluid is described by the Navier–Stokes–Fourier constitutive equations [2, p. 135],

$$q_i = -\kappa \frac{\partial T}{\partial x_i}, \tag{2.44}$$

$$\sigma_{ij} = {}^{\mathrm{r}}\sigma_{ij} + {}^{\mathrm{d}}\sigma_{ij}, \tag{2.45}$$

$${}^{\mathrm{r}}\sigma_{ij} = -p\delta_{ij}, \tag{2.46}$$

$${}^{\mathrm{d}}\sigma_{ij} = \lambda \frac{\partial v_k}{\partial x_k}\delta_{ji} + \mu^{\mathrm{F}} \left(\frac{\partial v_j}{\partial x_i} + \frac{\partial v_i}{\partial x_j} \right), \tag{2.47}$$

where κ denotes the thermal conductivity.

For an incompresible fluid, the constitutive equation for the specific entropy is given by [2, p. 132]

$$\eta = c \ln \left(\frac{T}{T_{\mathrm{ref}}} \right), \tag{2.48}$$

where c is the specific heat capacity and T_{ref} an arbitrary reference temperature.

2.3.4 Linear thermoelastic solid

The material behaviour of a linear thermoelastic solid is described by the following constitutive equations [2, p. 149]:

$$Q_i = -\kappa \frac{\partial T}{\partial X_i}, \tag{2.49}$$

$$S_{ij} = {}^{\mathrm{r}}S_{ij} + {}^{\mathrm{d}}S_{ij}, \tag{2.50}$$

$${}^{\mathrm{r}}S_{ij} = C_{ijkl} \left(E_{kl} - \alpha_{kl} \left(T - T_{\mathrm{ref}} \right) \right), \tag{2.51}$$

$${}^{\mathrm{d}}S_{ij} = 0, \tag{2.52}$$

$$\eta = c \ln \left(\frac{T}{T_{\mathrm{ref}}} \right) + \frac{1}{\rho_0} C_{ijkl} \alpha_{kl} E_{ij}, \tag{2.53}$$

with the stiffness tensor C_{ijkl} and the coefficients of thermal expansion α_{ij} for an isotropic body defined by

$$C_{ijkl} = \lambda \delta_{ij}\delta_{kl} + \mu \delta_{ik}\delta_{jl} + \mu \delta_{il}\delta_{jk}, \qquad \alpha_{ij} = \alpha \delta_{ij}. \tag{2.54}$$

3 Arbitrary Lagrangean–Eulerian form of balance equations in referential coordinates

For the monolithic solution method in this thesis the structure is modeled via balance equations in LAGRANGEan form. This approach is a classical one that is widely known and used successfully in structure mechanics. When it comes to fluid–structure interaction, the deforming structure is often surrounded by fluid. Note that the structure indeed deforms in spatial coordinates although solved in the reference configuration, i.e., in material coordinates on a temporarily fixed mesh.

The fluid domain is an open system described by a control volume fixed in space. This applies to an EULERian description in spatial coordinates where fluid enters and leaves the domain. However, the structure embedded in the fluid deforms and, thus, changes the boundary of the fluid domain in spatial coordinates.

The ALE approach deals with this phenomenon. In general, the fluid mesh moves arbitrarily. Since the mesh is fixed spatially at the edges of the control volume, the control volume is retained throughout the simulation in case of admissible mesh deformations. On the contrary, the fluid domain moves with the structure in spatial coordinates at the interface to the structure.

For instance, an ALE viewpoint is employed in combination with spatial coordinates and a partitioned solution procedure in [2, pp. 99–109]. If both fluid and structure are described in their current configuration, i.e., the fluid and structure domains deform, the setup of a monolithic algorithm is basically possible. However, during post-processing some effort has to be invested in tracking of the interface as it might be difficult to identify where the structure actually is located within the fluid.

For the monolithic approach in this thesis—having the structure equations in LAGRANGEan form on a fixed reference domain (material domain)—another approach is utilized. As in [21], the fluid domain is also transformed into its reference configuration which corresponds to the referential domain. Hence, the entire mesh does not have to be moved making it easy to identify the structure in material coordinates yet difficult to visualize the fluid results. In this chapter, therefore, the ALE form of balance equations in referential

coordinates are studied. First, a weak form is obtained for an incompressible, viscous fluid flow problem. Second, the weak form is applied to simulate a channel flow in order to assess the results qualitatively and quantitatively.

3.1 Weak form

A weak form of the considered PDEs is used for the finite element method. It can be generally generated by conducting three steps:

1. Choose appropriate balance equations.
2. Plug in suitable constitutive relations.
3. Multiply the obtained PDEs in their local form with test functions, integrate over the domain (integral form) and perform partial integration in order to *weaken* the required regularity of the solution.

First of all, the balance equations for an ALE viewpoint are determined. We begin with the balances of mass and linear momentum in EULERian form as introduced in Sect. 2.2,

$$\left.\frac{\partial \rho}{\partial t}\right|_{\boldsymbol{x}} + \frac{\partial \rho v_i}{\partial x_i} = 0, \tag{3.1}$$

$$\left.\frac{\partial \rho v_i}{\partial t}\right|_{\boldsymbol{x}} + \frac{\partial \rho v_j v_i}{\partial x_j} - \frac{\partial \sigma_{ji}}{\partial x_j} - \rho f_i = 0. \tag{3.2}$$

The fluid is assumed to be incompressible which means

$$\rho = \text{const.} \quad \forall\, t,\, \boldsymbol{x}. \tag{3.3}$$

Consequently, the mass balance, Eq. (3.1), reduces to

$$\frac{\partial v_i}{\partial x_i} = 0, \tag{3.4}$$

and the balance of linear momentum, Eq. (3.2), becomes

$$\rho \left.\frac{\partial v_i}{\partial t}\right|_{\boldsymbol{x}} + \rho v_j \frac{\partial v_i}{\partial x_j} - \frac{\partial \sigma_{ji}}{\partial x_j} - \rho f_i = 0. \tag{3.5}$$

At this point, we adopt the ALE viewpoint by the referential time derivative in Eq. (2.19),

$$\begin{aligned} \left.\frac{\partial v_i}{\partial t}\right|_{\boldsymbol{\chi}} &= \left.\frac{\partial v_i}{\partial t}\right|_{\boldsymbol{x}} + w_j \frac{\partial v_i}{\partial x_j} \\ \Leftrightarrow \left.\frac{\partial v_i}{\partial t}\right|_{\boldsymbol{x}} &= \left.\frac{\partial v_i}{\partial t}\right|_{\boldsymbol{\chi}} - w_j \frac{\partial v_i}{\partial x_j}. \end{aligned} \tag{3.6}$$

Using Eq. (3.6), the spatial time derivative in Eq. (3.5) is replaced by the referential time derivative such that we obtain

$$\rho \left.\frac{\partial v_i}{\partial t}\right|_{\boldsymbol{\chi}} + \rho \left(v_j - w_j\right) \frac{\partial v_i}{\partial x_j} - \frac{\partial \sigma_{ji}}{\partial x_j} - \rho f_i = 0. \tag{3.7}$$

Equation (3.7) represents the balance of linear momentum for an ALE viewpoint expressed in spatial coordinates.

As a constitutive equation for the CAUCHY stress, the NAVIER–STOKES's equation is chosen:

$$\sigma_{ji} = -p\delta_{ji} + \lambda \frac{\partial v_k}{\partial x_k}\delta_{ji} + \mu^{\mathrm{F}} \left(\frac{\partial v_j}{\partial x_i} + \frac{\partial v_i}{\partial x_j} \right). \tag{3.8}$$

Due to Eq. (3.4) the middle term is set to zero which yields

$$\sigma_{ji} = -p\delta_{ji} + \mu^{\mathrm{F}} \left(\frac{\partial v_j}{\partial x_i} + \frac{\partial v_i}{\partial x_j} \right). \tag{3.9}$$

Inserting Eq. (3.9) into the balance of linear momentum in Eq. (3.7) leads to

$$\rho \left.\frac{\partial v_i}{\partial t}\right|_{\boldsymbol{\chi}} + \rho \left(v_j - w_j\right) \frac{\partial v_i}{\partial x_j} + \frac{\partial p}{\partial x_i} - \mu^{\mathrm{F}} \frac{\partial^2 v_i}{\partial x_j \partial x_j} - \mu^{\mathrm{F}} \frac{\partial^2 v_j}{\partial x_i \partial x_j} - \rho f_i = 0. \tag{3.10}$$

In order to obtain the weak form, Eq. (3.10) is multiplied by a test function δv_i and integrated over the domain Ω^x such that

$$\int_{\Omega^x} \left(\rho \left.\frac{\partial v_i}{\partial t}\right|_{\boldsymbol{\chi}} + \rho \left(v_j - w_j\right) \frac{\partial v_i}{\partial x_j} + \frac{\partial p}{\partial x_i} - \mu^{\mathrm{F}} \frac{\partial^2 v_i}{\partial x_j \partial x_j} - \mu^{\mathrm{F}} \frac{\partial^2 v_j}{\partial x_i \partial x_j} - \rho f_i \right) \delta v_i \, \mathrm{d}v = 0. \tag{3.11}$$

Next, partial integration is applied to the terms with second order partial

derivatives to weaken the required regularity of v_i,

$$\int_{\Omega^x} \left(\left(\rho \left. \frac{\partial v_i}{\partial t} \right|_{\boldsymbol{\chi}} + \rho \left(v_j - w_j \right) \frac{\partial v_i}{\partial x_j} + \frac{\partial p}{\partial x_i} - \rho f_i \right) \delta v_i \right.$$
$$\left. + \mu^{\mathrm{F}} \frac{\partial v_i}{\partial x_j} \frac{\partial \delta v_i}{\partial x_j} + \mu^{\mathrm{F}} \frac{\partial v_j}{\partial x_i} \frac{\partial \delta v_i}{\partial x_j} \right) \mathrm{d}v$$
$$- \int_{\partial\Omega^x} \mu^{\mathrm{F}} \left(\frac{\partial v_i}{\partial x_j} + \frac{\partial v_j}{\partial x_i} \right) \delta v_i n_j \, \mathrm{d}a = 0. \tag{3.12}$$

The boundary of the spatial domain is split into two parts:

$$\partial\Omega^x = \Gamma^x = \Gamma^x_{\mathrm{D}} \cup \Gamma^x_{\mathrm{N}}, \tag{3.13}$$

where Γ^x_{D} is the part of the boundary on which DIRICHLET boundary conditions are imposed for the velocity, v_i, while Γ^x_{N} corresponds to NEUMANN boundary conditions. The function space for the test functions is chosen in such a way that $\delta v_i = 0$ on Γ^x_{D}, so the boundary integral vanishes on Γ^x_{D}. On the remaining boundary Γ^x_{N} we have

$$- \int_{\Gamma^x_{\mathrm{N}}} \mu^{\mathrm{F}} \left(\frac{\partial v_i}{\partial x_j} + \frac{\partial v_j}{\partial x_i} \right) \delta v_i n_j \, \mathrm{d}a = - \int_{\Gamma^x_{\mathrm{N}}} \left(\sigma_{ji} + p\delta_{ji} \right) \delta v_i n_j \, \mathrm{d}a. \tag{3.14}$$

Following the argumentation in [2, p. 81], the mechanical pressure is equal to the hydrostatic pressure for incompressible fluids,

$$- \frac{1}{3} \sigma_{kk} = p, \tag{3.15}$$

and, thus, the mechanical pressure can be prescribed on Γ^x_{N} by

$$t_i = \sigma_{ji} n_j = -p n_i, \tag{3.16}$$

in which t_i is the traction vector. As a consequence of that, the boundary integral in Eq. (3.14) and Eq. (3.12) vanishes also on Γ^x_{N}. This approach can be interpreted as a *zero shear stress* boundary condition [17, 37] since the shear stress of the fluid is indirectly assumed to be zero on the respective boundary.

The mass balance in Eq. (3.4) is likewise reformulated by multiplying with a test function δp and integrating over the domain Ω^x leading to

$$\int_{\Omega^x} \frac{\partial v_i}{\partial x_i} \delta p \, \mathrm{d}v = 0. \tag{3.17}$$

Equation (3.12) and Eq. (3.17) are still written in spatial coordinates. As

we want to examine the equations in referential coordinates in this chapter, we transform them by applying the transformation rules given in Eq. (2.11)-Eq. (2.12):

$$\frac{\partial v_i}{\partial x_i} = \frac{\partial v_i}{\partial \chi_k} \left(\hat{\boldsymbol{F}}^{-1}\right)_{ki}, \tag{3.18}$$

$$\frac{\partial v_i}{\partial x_j} = \frac{\partial v_i}{\partial \chi_k} \left(\hat{\boldsymbol{F}}^{-1}\right)_{kj}, \tag{3.19}$$

$$\frac{\partial p}{\partial x_i} = \frac{\partial p}{\partial \chi_k} \left(\hat{\boldsymbol{F}}^{-1}\right)_{ki}, \tag{3.20}$$

$$\frac{\partial v_i}{\partial x_j} \frac{\partial \delta v_i}{\partial x_j} = \frac{\partial v_i}{\partial \chi_k} \left(\hat{\boldsymbol{F}}^{-1}\right)_{kj} \frac{\partial \delta v_i}{\partial \chi_l} \left(\hat{\boldsymbol{F}}^{-1}\right)_{lj}, \tag{3.21}$$

$$\frac{\partial v_j}{\partial x_i} \frac{\partial \delta v_i}{\partial x_j} = \frac{\partial v_j}{\partial \chi_k} \left(\hat{\boldsymbol{F}}^{-1}\right)_{ki} \frac{\partial \delta v_i}{\partial \chi_l} \left(\hat{\boldsymbol{F}}^{-1}\right)_{lj}, \tag{3.22}$$

such that we obtain

$$\int_{\Omega^\chi} \frac{\partial v_i}{\partial \chi_k} \left(\hat{\boldsymbol{F}}^{-1}\right)_{ki} \delta p \hat{J} \, \mathrm{d}\hat{V} = 0, \tag{3.23}$$

$$\begin{aligned} \int_{\Omega^\chi} \Bigg(& \left(\rho \frac{\partial v_i}{\partial t}\bigg|_{\boldsymbol{\chi}} + \rho \left(v_j - w_j\right) \frac{\partial v_i}{\partial \chi_k} \left(\hat{\boldsymbol{F}}^{-1}\right)_{kj} + \frac{\partial p}{\partial \chi_k} \left(\hat{\boldsymbol{F}}^{-1}\right)_{ki} - \rho f_i \right) \delta v_i \\ & + \mu^{\mathrm{F}} \frac{\partial v_i}{\partial \chi_k} \left(\hat{\boldsymbol{F}}^{-1}\right)_{kj} \frac{\partial \delta v_i}{\partial \chi_l} \left(\hat{\boldsymbol{F}}^{-1}\right)_{lj} + \mu^{\mathrm{F}} \frac{\partial v_j}{\partial \chi_k} \left(\hat{\boldsymbol{F}}^{-1}\right)_{ki} \frac{\partial \delta v_i}{\partial \chi_l} \left(\hat{\boldsymbol{F}}^{-1}\right)_{lj} \Bigg) \hat{J} \, \mathrm{d}\hat{V} = 0. \end{aligned} \tag{3.24}$$

All field quantities in Eq. (3.23) and Eq. (3.24) are now defined in the referential domain Ω^χ which does not move. For the sake of legibility, a star notation as in Sect. 2.1 is omitted. Moreover, both forms are in the unit of power such that they can be added.

3.2 Study of a laminar channel flow

In order to verify the correctness of the weak form resulting from the summation of Eq. (3.23) and Eq. (3.24), it is applied to the problem of a laminar channel flow. The model setup and computation of the weak forms' solution is conducted by using the open-source packages developed under the FEniCS project [3].

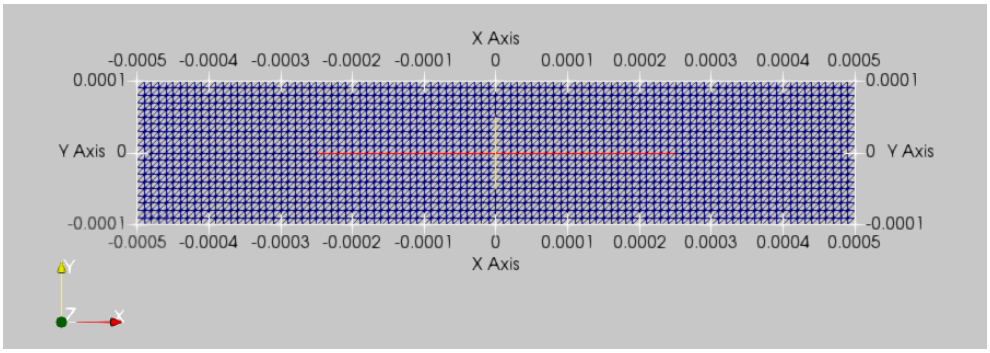

Fig. 3.1: Channel geometry and mesh

The time derivative in Eq. (3.24) is discretized by the backward EULER method:

$$\frac{\partial v_i}{\partial t} = \frac{v_i - v_i^0}{t - t^0} = \frac{v_i - v_i^0}{\Delta t}, \tag{3.25}$$

where v_i denotes the velocity at the current time step, v_i^0 the velocity at the previous time step and Δt the time increment of the current and the previous time step. Analogously, the mesh velocity w_j is discretized as partial derivative of the mesh displacement; see Eq. (2.20):

$$w_i = \frac{\partial d_i}{\partial t} = \frac{d_i - d_i^0}{\Delta t}. \tag{3.26}$$

As spatial discretization the FEM is chosen. The mesh constists of 4000 triangle elements. The channel geometry and the described mesh are shown in Fig. 3.1. The primitive variables v_i and p are solved monolithically by use of an LU decomposition and continuous linear ansatz functions for the primitive variables (trial functions) and the test functions. As the respective function spaces are the same for both trial and test functions, this corresponds to a GALKERIN type FEM.

The 2D channel flow problem is basically adopted from [2, p. 76-86] except that all physical quantities are expressed in SI units and the above weak form is considered. The model parameters are summarized in Table 3.1. At the beginning, the fluid rests under normal atmospheric pressure. Via DIRICHLET boundary conditions, the pressure p is increased on the left boundary linearly in the time interval from t^{start} until t^{bc} up to $p^{\text{in}}(t = t^{\text{bc}})$ while it is held constant on the right boundary at p^{out}. Therefore, a flow from left to right emerges. For the velocity, v_i, *no-slip* boundary conditions are applied on the upper and lower boundary of the channel and the inlet and outlet velocities are restricted to the channel axis. The volumetric force term, f_i, is neglected.

Table 3.1: Model parameters for laminar channel flow

Channel length (m)	0.001
Channel height (m)	0.0002
ρ (kg/m^3)	998.21
μ^{F} (Ns/m^2)	0.001
t^{start} (s)	0
t^{end} (s)	0.022
t^{bc} (s)	0.0001
Δt (s)	0.00001
$p^{\mathrm{in}}(t = t^{\mathrm{bc}})$ (Pa)	100400
p^{out} (Pa)	100000

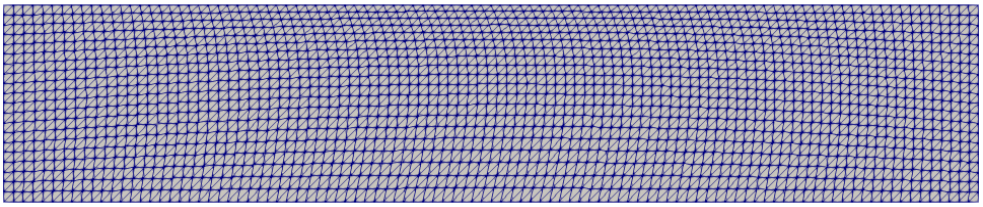

Fig. 3.2: Mesh deformation at $t = 0.02183$ s

The prescribed mesh displacement, d_i, is an arbitrary quadratic function in space vanishing on the boundaries of the control volume such that $\Gamma^x = \Gamma^\chi$. Besides, it is a harmonic in time with a high frequency referred to the actual flow problem. The mesh deformation at time $t = 0.02183$ s is shown in Fig. 3.2.

At this time instant, a steady-state solution of the fluid problem is obtained. The solution of the velocity in x-direction is illustrated in Fig. 3.3 (a) in the referential domain Ω^χ. Obviously, this representation is not suitable for the interpretation of the results since it depicts the velocity at each individually moving node. The appropriate way to present the results is in the spatial domain Ω^x, i.e., on a deformed mesh. The corresponding solution of the velocity in x-direction is illustrated in Fig. 3.3 (b). The results in Ω^x can be easily created from the results in the referential domain Ω^χ with the open-source data analysis and visualization application ParaView [4] by using the *Append Attributes* filter and the *Warp By Vector* functionality.

In the following the computed steady-state velocity profile in x-direction v_x^{ALE} along the channel height is considered in the middle of the channel. In

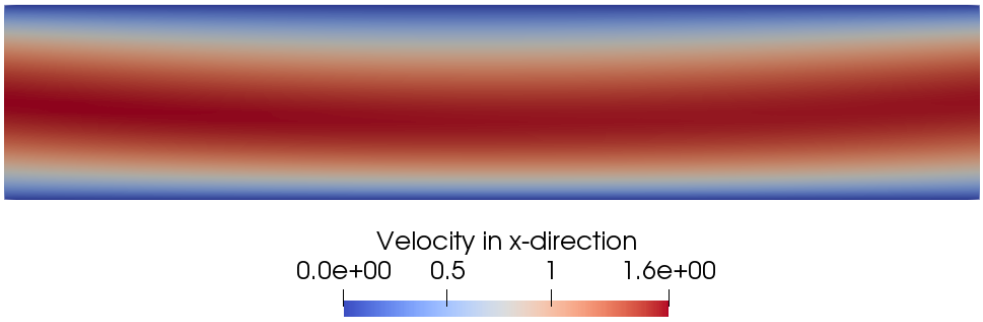

(a) in Ω^χ

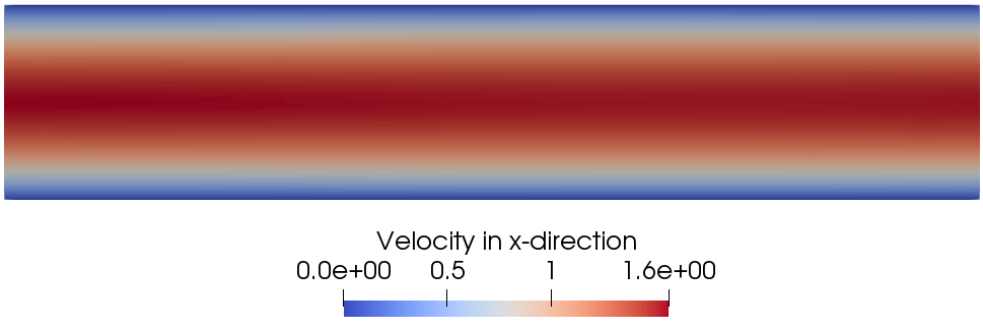

(b) in Ω^x

Fig. 3.3: Computed velocity fields in x-direction at $t = 0.02183$ s presented in different domains

Fig. 3.4 it is compared to a modified computation with half of the original time step size, an EULERian computation, v_x^{Euler}, based on Eq. (3.12) and the analytical solution v_x^{HP} of the HAGEN–POISEUILLE channel flow[1]. Obviously, the EULERian solution is almost identical to the analytical solution. However, the ALE solution is quite far away of both. For a smaller time step size, it approaches significantly to the analytical solution. Since at steady-state the acceleration of the fluid given in Eq. (3.25) becomes zero, the deviation of the ALE solution is caused by the backward EULER time discretization in Eq. (3.26). As a consequence of that, the time step size Δt should be always also selected with regard to the mesh velocity, i.e., it has to be small enough to resolve all time derivatives in the weak form.

Eventually, one might come to the idea not to prescribe the mesh displacement

[1]The derivation of the analytical solution is attached in Chap. A.

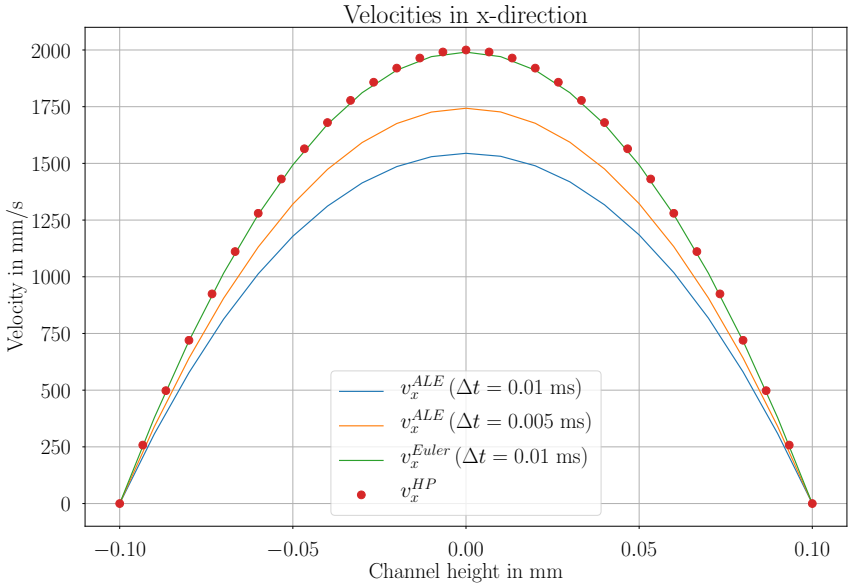

Fig. 3.4: Computed steady-state velocities in x-direction at $x = 0.5$ mm and $t = 0.02183$ s

d_i, but the equivalent mesh velocity w_i instead, such that the time discretization in Eq. (3.26) is not necessary in the weak form. Nevertheless, the mesh velocity has to be integrated to compute the mesh deformation gradient; see Eq. (2.5). The easiest way to realize this is to use the EULER–CAUCHY time integration such that

$$d_i = d_i^0 + w_i \Delta t, \tag{3.27}$$

where d_i^0 denotes the mesh displacement at the previous time step. The resulting plots of the steady-state velocity profile are identical to those presented in Fig. 3.4. Consequently, it seems that the utilized time derivation and integration schemes are equivalent. Thus, it can be concluded, that the choice of prescribing a mesh velocity or a mesh displacement does not affect the accuracy of the results.

4 Monolithic computational approach for fluid–structure interaction

In this chapter a monolithic solution method for the FSI of an incompressible, viscous fluid with a compressible, linear elastic structure is developed. The basic idea is adapted from [16]. However, the developed method differs in several aspects like the choice of equations in the weak form and the utilized discretization techniques. Furthermore, the method is applied and validated by comparing its results to numerically computed reference data of a benchmark setting described in [31]. For that purpose, the open-source computing platform FEniCS [3] is used. Finally, an alternative solution approach is presented.

4.1 Weak form

A monolithic approach is pursued in this thesis, i.e., both fluid and structure subproblems are combined into one problem over the whole domain. The fluid subproblem is defined on the fluid subdomain while the structure subproblem is defined on the structure subdomain. The two subproblems are combined by adding their respective weak forms such that a weak form in the whole domain is obtained. The fluid equations are expressed in referential coordinates using an ALE viewpoint whereas the structure problem is formulated in material coordinates with a LAGRANGEan viewpoint. Hence, both subproblems are described in their reference configuration on a fixed mesh.

For the monolithic formulation, a specific notation is introduced. Let the entire computational domain, $\tilde{\Omega}$, be described by *computational coordinates*, $\tilde{X}_i$, and let $\tilde{\Omega}$ be composed of the fluid and structure subdomains $\tilde{\Omega}_\mathrm{F}$ and $\tilde{\Omega}_\mathrm{S}$, respectively, such that

$$\tilde{\Omega} = \tilde{\Omega}_\mathrm{F} \cup \tilde{\Omega}_\mathrm{S}, \qquad \tilde{\Omega}_\mathrm{F} = \Omega_\mathrm{F}^\chi, \qquad \tilde{\Omega}_\mathrm{S} = \Omega_\mathrm{S}^X, \qquad \tilde{X}_i = \begin{cases} \chi_i & \text{in } \tilde{\Omega}_\mathrm{F}, \\ X_i & \text{in } \tilde{\Omega}_\mathrm{S}. \end{cases} \tag{4.1}$$

Then three field quantities ($\tilde{p}$, $\tilde{v}_i$, $\tilde{u}_i$) are defined in $\tilde{\Omega}$:

$$\tilde{p} = \begin{cases} p & \text{in } \tilde{\Omega}_\mathrm{F}, \\ \bar{p} & \text{in } \tilde{\Omega}_\mathrm{S}, \end{cases} \qquad \tilde{v}_i = v_i \quad \text{in } \tilde{\Omega}, \qquad \tilde{u}_i = \begin{cases} d_i & \text{in } \tilde{\Omega}_\mathrm{F}, \\ u_i & \text{in } \tilde{\Omega}_\mathrm{S}, \end{cases} \tag{4.2}$$

where $\bar{p}$ is an artificial pressure. The introduced field quantities ($\tilde{p}$, $\tilde{v}_i$, $\tilde{u}_i$) constitute the unknowns in the resulting system of equations. An FEM is applied to solve the whole system for all the unknowns simultaneously. Hence, weak forms have to be defined in both subdomains for the computation of the respective unknowns. Additionally, from the upper definitions a computational deformation gradient, $\tilde{F}_{ij}$, is deduced such that

$$\tilde{F}_{ij} = \begin{cases} \hat{F}_{ij} & \text{in } \tilde{\Omega}_\mathrm{F}, \\ F_{ij} & \text{in } \tilde{\Omega}_\mathrm{S}, \end{cases} \qquad \text{with} \qquad \tilde{J} = \begin{cases} \hat{J} & \text{in } \tilde{\Omega}_\mathrm{F}, \\ J & \text{in } \tilde{\Omega}_\mathrm{S}. \end{cases} \tag{4.3}$$

This definition is allowed if $\tilde{u}_i$ is continuous. Therefore, continuous basis functions have to be chosen for $\tilde{u}_i$. If the basis functions for $\tilde{v}_i$ are also continuous, the overall velocity field $\tilde{v}_i$ is continuous. Particularly, on the interface $\tilde{\Gamma}_\mathrm{I} = \tilde{\Omega}_\mathrm{F} \cap \tilde{\Omega}_\mathrm{S}$ the velocity is continuous, i.e., both fluid and structure have the same velocity on $\tilde{\Gamma}_\mathrm{I}$ and—since the displacement field $\tilde{u}_i$ is continuous—also on Γ_I^x. This means that the first interaction condition, a *no-slip* boundary condition between fluid and structure, is already fulfilled by choosing continuous ansatz functions for $\tilde{v}_i$ and $\tilde{u}_i$.

4.1.1 Weak form in the fluid subdomain

In the fluid subdomain the mass balance for an incompressible fluid is exploited. Its integral form is given by Eq. (3.23) and reads in the specific notation for the monolithic problem

$$\int_{\tilde{\Omega}_\mathrm{F}} \frac{\partial \tilde{v}_i}{\partial \tilde{X}_k} \left(\tilde{\boldsymbol{F}}^{-1} \right)_{ki} \delta\tilde{p} \tilde{J} \, \mathrm{d}\tilde{V} = 0, \tag{4.4}$$

where $\delta\tilde{p}$ is the test function for the pressure and $\mathrm{d}\tilde{V}$ the volume element in computational coordinates, $\tilde{X}_i$.

Moreover, the balance of linear momentum is evaluated. In order to obtain its weak form, we begin with the balance of linear momentum for the ALE viewpoint in spatial coordinates with incorporated NAVIER-STOKES's equation as in Eq. (3.10):

$$\rho^\mathrm{F} \left. \frac{\partial v_i}{\partial t} \right|_{\boldsymbol{\chi}} + \rho^\mathrm{F} \left(v_j - w_j \right) \frac{\partial v_i}{\partial x_j} + \frac{\partial p}{\partial x_i} - \mu^\mathrm{F} \frac{\partial^2 v_i}{\partial x_j \partial x_j} - \mu^\mathrm{F} \frac{\partial^2 v_j}{\partial x_i \partial x_j} - \rho^\mathrm{F} f_i = 0. \tag{4.5}$$

Equation (4.5) is multiplied by a test function $\delta\tilde{v}_i$ for the velocity and integrated

over the fluid subdomain in spatial coordinates such that we get

$$\int_{\Omega_{\mathrm{F}}^x} \left(\rho^{\mathrm{F}} \left. \frac{\partial v_i}{\partial t} \right|_{\boldsymbol{\chi}} + \rho^{\mathrm{F}} \left(v_j - w_j \right) \frac{\partial v_i}{\partial x_j} - \rho^{\mathrm{F}} f_i \right. \\ \left. + \frac{\partial p}{\partial x_i} - \mu^{\mathrm{F}} \frac{\partial^2 v_i}{\partial x_j \partial x_j} - \mu^{\mathrm{F}} \frac{\partial^2 v_j}{\partial x_i \partial x_j} \right) \delta \tilde{v}_i \, \mathrm{d}v = 0. \tag{4.6}$$

Unlike the procedure in Chap. 3, the pressure gradient and the terms containing second derivatives are partially integrated. This leads to

$$\int_{\Omega_{\mathrm{F}}^x} \left(\left(\rho^{\mathrm{F}} \left. \frac{\partial v_i}{\partial t} \right|_{\boldsymbol{\chi}} + \rho^{\mathrm{F}} \left(v_j - w_j \right) \frac{\partial v_i}{\partial x_j} - \rho^{\mathrm{F}} f_i \right) \delta \tilde{v}_i \right. \\ \left. - p \frac{\partial \delta \tilde{v}_i}{\partial x_i} + \mu^{\mathrm{F}} \frac{\partial v_i}{\partial x_j} \frac{\partial \delta \tilde{v}_i}{\partial x_j} + \mu^{\mathrm{F}} \frac{\partial v_j}{\partial x_i} \frac{\partial \delta \tilde{v}_i}{\partial x_j} \right) \mathrm{d}v \\ - \int_{\Gamma_{\mathrm{F}}^x} \left(- p \delta_{ij} + \mu^{\mathrm{F}} \left(\frac{\partial v_i}{\partial x_j} + \frac{\partial v_j}{\partial x_i} \right) \right) \delta \tilde{v}_i n_j^{\mathrm{F}} \, \mathrm{d}a = 0. \tag{4.7}$$

Due to Eq. (3.9) the boundary integral can be written as

$$- \int_{\Gamma_{\mathrm{F}}^x} \sigma_{ji}^{\mathrm{F}} n_j^{\mathrm{F}} \delta \tilde{v}_i \, \mathrm{d}a = - \int_{\Gamma_{\mathrm{F}}^x} t_i^{\mathrm{F}} \delta \tilde{v}_i \, \mathrm{d}a, \tag{4.8}$$

where t_i^{F} is the traction vector on the boundary of the fluid subdomain. The boundary of the fluid subdomain is split into the following parts:

$$\Gamma_{\mathrm{F}}^x = \Gamma_{\mathrm{F,D,v}}^x \cup \Gamma_{\mathrm{F,N,v}}^x \cup \Gamma_{\mathrm{I}}^x, \tag{4.9}$$

where $\Gamma_{\mathrm{F,D,v}}^x$ is the part with DIRICHLET boundary conditions applied for the velocity and $\Gamma_{\mathrm{F,N,v}}^x$ the remaining boundary with NEUMANN boundary conditions for the velocity, that is not part of the interface Γ_{I}^x between the fluid and structure subdomains. The test function $\delta \tilde{v}_i$ vanishes on $\Gamma_{\mathrm{F,D,v}}^x$ such that the weak form becomes

$$\int_{\Omega_{\mathrm{F}}^x} \left(\left(\rho^{\mathrm{F}} \left. \frac{\partial v_i}{\partial t} \right|_{\boldsymbol{\chi}} + \rho^{\mathrm{F}} \left(v_j - w_j \right) \frac{\partial v_i}{\partial x_j} - \rho^{\mathrm{F}} f_i \right) \delta \tilde{v}_i - p \frac{\partial \delta \tilde{v}_i}{\partial x_i} + \mu^{\mathrm{F}} \frac{\partial v_i}{\partial x_j} \frac{\partial \delta \tilde{v}_i}{\partial x_j} \right. \\ \left. + \mu^{\mathrm{F}} \frac{\partial v_j}{\partial x_i} \frac{\partial \delta \tilde{v}_i}{\partial x_j} \right) \mathrm{d}v - \int_{\Gamma_{\mathrm{F,N,v}}^x} t_i^{\mathrm{F}} \delta \tilde{v}_i \, \mathrm{d}a - \int_{\Gamma_{\mathrm{I}}^x} t_i^{\mathrm{F}} \delta \tilde{v}_i \, \mathrm{d}a = 0. \tag{4.10}$$

The first two integrals are transformed into referential coordinates by applying

the transformation rules given in Eq. (2.11)-Eq. (2.12) such that

$$\int_{\Omega_{\mathrm{F}}^{\chi}} \Bigg(\Bigg(\rho^{\mathrm{F}} \frac{\partial v_i}{\partial t}\bigg|_{\boldsymbol{\chi}} + \rho^{\mathrm{F}} \left(v_j - w_j\right) \frac{\partial v_i}{\partial \chi_k} \left(\hat{\boldsymbol{F}}^{-1}\right)_{kj} - \rho^{\mathrm{F}} f_i \Bigg) \delta\tilde{v}_i - p \frac{\partial \delta\tilde{v}_i}{\partial \chi_k} \left(\hat{\boldsymbol{F}}^{-1}\right)_{ki} + \mu^{\mathrm{F}} \frac{\partial v_i}{\partial \chi_k} \left(\hat{\boldsymbol{F}}^{-1}\right)_{kj} \frac{\partial \delta\tilde{v}_i}{\partial \chi_l} \left(\hat{\boldsymbol{F}}^{-1}\right)_{lj} + \mu^{\mathrm{F}} \frac{\partial v_j}{\partial \chi_k} \left(\hat{\boldsymbol{F}}^{-1}\right)_{ki} \frac{\partial \delta\tilde{v}_i}{\partial \chi_l} \left(\hat{\boldsymbol{F}}^{-1}\right)_{lj} \Bigg) \hat{J} \, \mathrm{d}\hat{V} - \int_{\Gamma_{\mathrm{F,N,v}}^{\chi}} \hat{t}_i^{\mathrm{F}} \delta\tilde{v}_i \, \mathrm{d}\hat{A} - \int_{\Gamma_{\mathrm{I}}^{x}} t_i^{\mathrm{F}} \delta\tilde{v}_i \, \mathrm{d}a = 0, \tag{4.11}$$

with

$$\begin{aligned} - \int_{\Gamma_{\mathrm{F,N,v}}^{\chi}} \hat{t}_i^{\mathrm{F}} \delta\tilde{v}_i \, \mathrm{d}\hat{A} &= - \int_{\Gamma_{\mathrm{F,N,v}}^{\chi}} \hat{\sigma}_{ji}^{\mathrm{F}} \hat{N}_k^{\mathrm{F}} \left(\hat{\boldsymbol{F}}^{-1}\right)_{kj} \hat{J} \delta\tilde{v}_i \, \mathrm{d}\hat{A} \\ &= - \int_{\Gamma_{\mathrm{F,N,v}}^{x}} \sigma_{ji}^{\mathrm{F}} n_j^{\mathrm{F}} \delta\tilde{v}_i \, \mathrm{d}a = - \int_{\Gamma_{\mathrm{F,N,v}}^{x}} t_i^{\mathrm{F}} \delta\tilde{v}_i \, \mathrm{d}a. \end{aligned} \tag{4.12}$$

The boundary integral on the interface Γ_{I}^{x} is retained in spatial coordinates since it will be later applied for the second interaction condition, the equilibrium of forces, in spatial coordinates. As the time derivative of the velocity in Eq. (4.11) is now defined in referential coordinates, the vertical bar notation is dropped. In addition, the mesh velocity, w_j, is replaced by the time derivative of the mesh displacement, d_j, such that the weak form reads in the specific notation for the monolithic problem

$$\int_{\tilde{\Omega}_{\mathrm{F}}} \Bigg(\Bigg(\rho^{\mathrm{F}} \frac{\partial \tilde{v}_i}{\partial t} + \rho^{\mathrm{F}} \left(\tilde{v}_j - \frac{\partial \tilde{u}_j}{\partial t}\right) \frac{\partial \tilde{v}_i}{\partial \tilde{X}_k} \left(\tilde{\boldsymbol{F}}^{-1}\right)_{kj} - \rho^{\mathrm{F}} f_i \Bigg) \delta\tilde{v}_i - \tilde{p} \frac{\partial \delta\tilde{v}_i}{\partial \tilde{X}_k} \left(\tilde{\boldsymbol{F}}^{-1}\right)_{ki} + \mu^{\mathrm{F}} \frac{\partial \tilde{v}_i}{\partial \tilde{X}_k} \left(\tilde{\boldsymbol{F}}^{-1}\right)_{kj} \frac{\partial \delta\tilde{v}_i}{\partial \tilde{X}_l} \left(\tilde{\boldsymbol{F}}^{-1}\right)_{lj} + \mu^{\mathrm{F}} \frac{\partial \tilde{v}_j}{\partial \tilde{X}_k} \left(\tilde{\boldsymbol{F}}^{-1}\right)_{ki} \frac{\partial \delta\tilde{v}_i}{\partial \tilde{X}_l} \left(\tilde{\boldsymbol{F}}^{-1}\right)_{lj} \Bigg) \tilde{J} \, \mathrm{d}\tilde{V} - \int_{\tilde{\Gamma}_{\mathrm{F,N,v}}} \tilde{t}_i^{\mathrm{F}} \delta\tilde{v}_i \, \mathrm{d}\tilde{A} - \int_{\Gamma_{\mathrm{I}}^{x}} t_i^{\mathrm{F}} \delta\tilde{v}_i \, \mathrm{d}a = 0. \tag{4.13}$$

As a third equation, a form for the mesh displacement d_i, respectively, $\tilde{u}_i$ is needed in the fluid subdomain. It is desired that

$$d_i = u_i \text{ on } \tilde{\Gamma}_{\mathrm{I}}, \qquad d_i = 0 \text{ on } \tilde{\Gamma}_{\mathrm{F}} \setminus \tilde{\Gamma}_{\mathrm{I}}. \tag{4.14}$$

Apart from these conditions, the mesh motion is allowed to be arbitrary as long as a good mesh quality is preserved. There exists a great number of different equations for the mesh displacement; see, for example, [35, p. 24-27] and the references cited therein. A common approach is to treat the mesh as a solid

and solve it with a linear elastic constitutive model. Another approach is the harmonic mesh motion model which is used in this thesis. It reads in its local formulation

$$-\frac{\partial}{\partial \chi_j}\left(\alpha^{\mathrm{disp}}\frac{\partial d_i}{\partial \chi_j}\right)=0. \tag{4.15}$$

The mesh motion coefficient, $\alpha^{\mathrm{disp}}>0$, can be interpreted as a specific stiffness of the mesh motion problem. Since the mesh motion problem is solved for d_i, respectively, $\tilde{u}_i$ in the fluid subdomain, a high stiffness might also affect $\tilde{u}_i$ in the structure subdomain, which is equal to the displacement u_i of the structure. Certainly, this impact has to be eliminated. Hence, α^{disp} should be generally chosen small. If α^{disp} is a constant, the mesh motion problem can only deal with moderate fluid mesh deformations [36]. Larger deformations cause too large distortions of the fluid mesh elements leading to values for the determinant of the mesh deformation gradient, $\hat{J}$, which are close to zero or even negative. Especially, the latter case has to be avoided since $\hat{J}$ has to be positive, i.e. $\hat{J}>0$ in $\Omega_{\mathrm{F}}^{\chi}$, by definition of the mesh deformation gradient which would otherwise not be a bijective mapping from $\Omega_{\mathrm{F}}^{\chi}$ to Ω_{F}^{x}. This problem relates to both harmonic and linear elastic mesh motion models. The fluid mesh distortion increases especially near the interface to the structure subdomain. Therefore, several authors propose position-dependent formulations for α^{disp} measuring the distance to the interface to increase the stiffness locally ([35, p. 26], [27, p. 19]). Another approach for local stiffening is based on the evaluation of the numerical value of $\hat{J}$ [28]. In this thesis α^{disp} is constructed such that the stiffness is increased only around a small number of points within the fluid subdomain. If local stiffening is solely required around one point, we choose

$$\alpha^{\mathrm{disp}}=\frac{\varepsilon}{(\beta R)^{\gamma}}, \tag{4.16}$$

where R is the distance to the point and β, γ, ε are positive constants which have to be determined for the specific problem.

In order to obtain the weak form of Eq. (4.15), we multiply it with a test function $\delta\tilde{u}_i$ for the displacement and integrate over the fluid subdomain in referential coordinates such that we get

$$-\int_{\Omega_{\mathrm{F}}^{\chi}}\frac{\partial}{\partial \chi_j}\left(\alpha^{\mathrm{disp}}\frac{\partial d_i}{\partial \chi_j}\right)\delta\tilde{u}_i\,\mathrm{d}\hat{V}=0. \tag{4.17}$$

Partial integration leads to

$$\int_{\Omega_{\mathrm{F}}^{\chi}}\alpha^{\mathrm{disp}}\frac{\partial d_i}{\partial \chi_j}\frac{\partial \delta\tilde{u}_i}{\partial \chi_j}\,\mathrm{d}\hat{V}-\int_{\Gamma_{\mathrm{I}}^{\chi}}\alpha^{\mathrm{disp}}\frac{\partial d_i}{\partial \chi_j}\delta\tilde{u}_i\hat{N}_j\,\mathrm{d}\hat{A}=0. \tag{4.18}$$

Due to Eq. (4.14) the boundary integral becomes zero on the entire boundary of the fluid subdomain except of $\Gamma_{\mathrm{I}}^{\chi} = \tilde{\Gamma}_{\mathrm{I}}$. Since on the interface $\tilde{\Gamma}_{\mathrm{I}}$ the mesh displacement d_i is supposed to be prescribed by the displacement of the structure u_i, the mesh deformation coefficient α^{disp} has to be chosen so small that the influence of the fluid mesh stiffness on the structure deformation becomes negligible. Hence, also the boundary integral in Eq. (4.18) is negligible and, therefore, omitted in the following. Within the monolithic problem, the weak form then reads

$$\int_{\tilde{\Omega}_{\mathrm{F}}} \alpha^{\mathrm{disp}} \frac{\partial \tilde{u}_i}{\partial \tilde{X}_j} \frac{\partial \delta\tilde{u}_i}{\partial \tilde{X}_j} \,\mathrm{d}\tilde{V} = 0. \tag{4.19}$$

With the abbreviated notation for spatial derivatives in computational coordinates $\frac{\partial(\,)_i}{\partial \tilde{X}_j} = (\,)_{i,j}$, the forms in the fluid subdomain, i.e., Eq. (4.4), Eq. (4.13) and Eq. (4.19), are summarized:

$$\int_{\tilde{\Omega}_{\mathrm{F}}} \tilde{v}_{i,k} \left(\tilde{\boldsymbol{F}}^{-1}\right)_{ki} \delta\tilde{p}\tilde{J} \,\mathrm{d}\tilde{V} = 0, \tag{4.20}$$

$$\begin{aligned}
&\int_{\tilde{\Omega}_{\mathrm{F}}} \Bigg(\left(\rho^{\mathrm{F}} \frac{\partial \tilde{v}_i}{\partial t} + \rho^{\mathrm{F}} \left(\tilde{v}_j - \frac{\partial \tilde{u}_j}{\partial t} \right) \tilde{v}_{i,k} \left(\tilde{\boldsymbol{F}}^{-1}\right)_{kj} - \rho^{\mathrm{F}} f_i \right) \delta\tilde{v}_i - \tilde{p}\delta\tilde{v}_{i,k} \left(\tilde{\boldsymbol{F}}^{-1}\right)_{ki} \\
&+ \mu^{\mathrm{F}} \left(\tilde{v}_{i,k} \left(\tilde{\boldsymbol{F}}^{-1}\right)_{kj} + \tilde{v}_{j,k} \left(\tilde{\boldsymbol{F}}^{-1}\right)_{ki} \right) \delta\tilde{v}_{i,l} \left(\tilde{\boldsymbol{F}}^{-1}\right)_{lj} \Bigg) \tilde{J} \,\mathrm{d}\tilde{V} \\
&- \int_{\tilde{\Gamma}_{\mathrm{F,N,v}}} \tilde{t}_i^{\mathrm{F}} \delta\tilde{v}_i \,\mathrm{d}\tilde{A} - \int_{\Gamma_{\mathrm{I}}^{x}} t_i^{\mathrm{F}} \delta\tilde{v}_i \,\mathrm{d}a = 0,
\end{aligned} \tag{4.21}$$

$$\int_{\tilde{\Omega}_{\mathrm{F}}} \alpha^{\mathrm{disp}} \tilde{u}_{i,j} \delta\tilde{u}_{i,j} \,\mathrm{d}\tilde{V} = 0. \tag{4.22}$$

4.1.2 Weak form in the structure subdomain

Appropriate equations have to be determined for the field quantities ($\tilde{p}$, $\tilde{v}_i$, $\tilde{u}_i$) also in the structure subdomain. Since the pressure p is not considered in the St. Venant–Kirchhoff constitutive model, an artificial pressure, $\bar{p}$, is defined. This artificial pressure does not have any meaning for the actual FSI. Still, it is necessary to have an equation for $\tilde{p}$ in $\tilde{\Omega}_{\mathrm{S}}$ to formulate a monolithic problem in $\tilde{\Omega}$.

There exist approaches to employ the physical pressure p in monolithic methods; see, for instance, [16]. However, these approaches are limited to

incompressible structures for which an additional physically meaningful equation can be found in order to compute the pressure. The incompressibility is exploited by postulating[1] $J = 1$ in an integral form, and the pressure is included in the constitutive relation.

As it is desired to find a solution method for compressible structures, an arbitrary equation is necessary for the artificial pressure $\bar{p}$. Similarly to the mesh motion problem in the fluid subdomain, we pose an auxiliary LAPLACE problem for $\bar{p}$, generate the integral form in material coordinates and apply integration by parts such that we obtain

$$\int_{\Omega_{\mathrm{S}}^X} \alpha^{\mathrm{pres}} \frac{\partial \bar{p}}{\partial X_j} \frac{\partial \delta\tilde{p}}{\partial X_j} \,\mathrm{d}V - \int_{\Gamma_{\mathrm{I}}^X \cup \Gamma_{\mathrm{S,N,p}}^X} \alpha^{\mathrm{pres}} \frac{\partial \bar{p}}{\partial X_j} \delta\tilde{p} N_j \,\mathrm{d}A = 0. \tag{4.23}$$

The artificial pressure coefficient α^{pres} is introduced to reduce the impact of this weak form on the equations for the physical pressure p in the fluid subdomain. Furthermore, we demand that

$$\bar{p} = p \text{ on } \Gamma_{\mathrm{I}}^X = \tilde{\Gamma}_{\mathrm{I}}, \qquad \frac{\partial \bar{p}}{\partial X_j} = 0 \text{ on } \Gamma_{\mathrm{S,N,p}}^X = \Gamma_{\mathrm{S}}^X \setminus \Gamma_{\mathrm{I}}^X. \tag{4.24}$$

Hence, $\alpha^{\mathrm{pres}} > 0$ has to be a small constant, the boundary integral in Eq. (4.23) disappears on $\Gamma_{\mathrm{S,N,p}}^X$ and it can be neglected on Γ_{I}^X such that the weak form reads in the monolithic notation

$$\int_{\tilde{\Omega}_{\mathrm{S}}} \alpha^{\mathrm{pres}} \frac{\partial \tilde{p}}{\partial \tilde{X}_j} \frac{\partial \delta\tilde{p}}{\partial \tilde{X}_j} \,\mathrm{d}\tilde{V} = 0. \tag{4.25}$$

For the velocity v_i of the structure, the balance of linear momentum for the LAGRANGEan viewpoint is evaluated in material coordinates; see Eq. (2.32):

$$\rho_0^{\mathrm{S}} \left.\frac{\partial v_i}{\partial t}\right|_{\boldsymbol{X}} - \frac{\partial P_{ki}}{\partial X_k} - \rho_0^{\mathrm{S}} f_i = 0. \tag{4.26}$$

The weak form is deduced in the material domain, such that the vertical bar notation can be omitted:

$$\int_{\Omega_{\mathrm{S}}^X} \left(\rho_0^{\mathrm{S}} \frac{\partial v_i}{\partial t} - \frac{\partial P_{ki}}{\partial X_k} - \rho_0^{\mathrm{S}} f_i \right) \delta\tilde{v}_i \,\mathrm{d}V = 0. \tag{4.27}$$

[1] This can be deduced directly from the balance of mass in Eq. (2.31) for $\rho = \rho_0$.

Integration by parts of the divergence term gives

$$\int_{\Omega_{\mathrm{S}}^X} \left(\rho_0^{\mathrm{S}} \frac{\partial v_i}{\partial t} \delta\tilde{v}_i + P_{ki} \frac{\partial \delta\tilde{v}_i}{\partial X_k} - \rho_0^{\mathrm{S}} f_i \delta\tilde{v}_i \right) \mathrm{d}V - \int_{\Gamma_{\mathrm{I}}^X \cup \Gamma_{\mathrm{S,N,v}}^X} P_{ki} N_k^{\mathrm{S}} \delta\tilde{v}_i \, \mathrm{d}A = 0, \tag{4.28}$$

where $\Gamma_{\mathrm{S,N,v}}^X$ is the boundary with NEUMANN conditions applied for the velocity which does not belong to the interface $\Gamma_{\mathrm{I}}^X = \tilde{\Gamma}_{\mathrm{I}}$. Whereas the NEUMANN boundary conditions are usually deployed in material coordinates for structures, the interaction condition is expressed in spatial coordinates. Therefore, the boundary integral in Eq. (4.28) is split into two parts and the integral over Γ_{I}^X is transformed into spatial coordinates by means of the definition of the nominal stress, Eq. (2.33), and the transformation rule in Eq. (2.13):

$$\begin{aligned} -\int_{\Gamma_{\mathrm{I}}^X} P_{ki} N_k^{\mathrm{S}} \delta\tilde{v}_i \, \mathrm{d}A &= -\int_{\Gamma_{\mathrm{I}}^X} \left(\boldsymbol{F}^{-1} \right)_{kj} \sigma_{ji}^{\mathrm{S}} J N_k^{\mathrm{S}} \delta\tilde{v}_i \, \mathrm{d}A \\ &= -\int_{\Gamma_{\mathrm{I}}^x} \sigma_{ji}^{\mathrm{S}} \delta\tilde{v}_i n_j^{\mathrm{S}} \, \mathrm{d}a = -\int_{\Gamma_{\mathrm{I}}^x} t_i^{\mathrm{S}} \delta\tilde{v}_i \, \mathrm{d}a. \end{aligned} \tag{4.29}$$

Moreover, a traction vector in material and computational coordinates is defined as $\tilde{t}_i^{\mathrm{S}} = P_{ki} N_k^{\mathrm{S}}$ such that the weak form becomes

$$\begin{aligned} &\int_{\tilde{\Omega}_{\mathrm{S}}} \left(\rho_0^{\mathrm{S}} \frac{\partial \tilde{v}_i}{\partial t} \delta\tilde{v}_i + P_{ki} \frac{\partial \delta\tilde{v}_i}{\partial \tilde{X}_k} - \rho_0^{\mathrm{S}} f_i \delta\tilde{v}_i \right) \mathrm{d}\tilde{V} \\ &- \int_{\tilde{\Gamma}_{\mathrm{S,N,v}}} \tilde{t}_i^{\mathrm{S}} \delta\tilde{v}_i \, \mathrm{d}\tilde{A} - \int_{\Gamma_{\mathrm{I}}^x} t_i^{\mathrm{S}} \delta\tilde{v}_i \, \mathrm{d}a = 0, \end{aligned} \tag{4.30}$$

where $\mathrm{d}\tilde{A}$ represents an area element in computational coordinates.

The displacement of the structure, u_i, is determined by Eq. (2.17),

$$\frac{\partial u_i}{\partial t} = v_i, \tag{4.31}$$

such that the corresponding integral form is given by

$$\int_{\Omega_{\mathrm{S}}^X} \left(\frac{\partial u_i}{\partial t} - v_i \right) \delta\tilde{u}_i \, \mathrm{d}V = 0 \Rightarrow \int_{\tilde{\Omega}_{\mathrm{S}}} \left(\frac{\partial \tilde{u}_i}{\partial t} - \tilde{v}_i \right) \delta\tilde{u}_i \, \mathrm{d}\tilde{V} = 0. \tag{4.32}$$

Below, the forms in the structure subdomain, i.e., Eq. (4.25), Eq. (4.30) and Eq. (4.32), are summarized:

$$\int_{\tilde{\Omega}_{\mathrm{S}}} \alpha^{\mathrm{pres}} \tilde{p}_{,j} \delta\tilde{p}_{,j} \, \mathrm{d}\tilde{V} = 0, \tag{4.33}$$

$$\int_{\tilde{\Omega}_\mathrm{S}} \left(\rho_0^\mathrm{S} \frac{\partial \tilde{v}_i}{\partial t} \delta\tilde{v}_i + P_{ki} \delta\tilde{v}_{i,k} - \rho_0^\mathrm{S} f_i \delta\tilde{v}_i \right) \mathrm{d}\tilde{V}$$
$$- \int_{\tilde{\Gamma}_{\mathrm{S,N,v}}} \tilde{t}_i^\mathrm{S} \delta\tilde{v}_i \, \mathrm{d}\tilde{A} - \int_{\Gamma_\mathrm{I}^x} t_i^\mathrm{S} \delta\tilde{v}_i \, \mathrm{d}a = 0, \tag{4.34}$$
$$\int_{\tilde{\Omega}_\mathrm{S}} \left(\frac{\partial \tilde{u}_i}{\partial t} - \tilde{v}_i \right) \delta\tilde{u}_i \, \mathrm{d}\tilde{V} = 0. \tag{4.35}$$

4.1.3 Weak form in the whole domain

The monolithic problem is formulated in the whole domain $\tilde{\Omega}$. Thus, the determined forms in both subdomains are added to one global weak form. Before, all equations are written in the same unit. Equation (4.20), Eq. (4.21) and Eq. (4.34) are already expressed in the unit of power. The units of α^disp and α^pres in Eq. (4.22) and Eq. (4.33), respectively, are defined in such a way that the particular equations are also expressed in the unit of power. However, Eq. (4.35) is not given in the unit of power. Hence, it is multiplied by the mass density of the fluid ρ^F and divided by $(\Delta t)^2$ since both constants represent characteristic quantities. The overall weak form for the monolithic FSI problem then reads

$$\int_{\tilde{\Omega}_\mathrm{F}} \tilde{v}_{i,k} \left(\tilde{\boldsymbol{F}}^{-1} \right)_{ki} \delta\tilde{p} \tilde{J} \, \mathrm{d}\tilde{V} + \int_{\tilde{\Omega}_\mathrm{S}} \alpha^\mathrm{pres} \tilde{p}_{,j} \delta\tilde{p}_{,j} \, \mathrm{d}\tilde{V}$$
$$+ \int_{\tilde{\Omega}_\mathrm{F}} \Bigg(\Bigg(\rho^\mathrm{F} \frac{\partial \tilde{v}_i}{\partial t} + \rho^\mathrm{F} \left(\tilde{v}_j - \frac{\partial \tilde{u}_j}{\partial t} \right) \tilde{v}_{i,k} \left(\tilde{\boldsymbol{F}}^{-1} \right)_{kj} - \rho^\mathrm{F} f_i \Bigg) \delta\tilde{v}_i$$
$$- \tilde{p} \delta\tilde{v}_{i,k} \left(\tilde{\boldsymbol{F}}^{-1} \right)_{ki} + \mu^\mathrm{F} \left(\tilde{v}_{i,k} \left(\tilde{\boldsymbol{F}}^{-1} \right)_{kj} + \tilde{v}_{j,k} \left(\tilde{\boldsymbol{F}}^{-1} \right)_{ki} \right) \delta\tilde{v}_{i,l} \left(\tilde{\boldsymbol{F}}^{-1} \right)_{lj} \Bigg) \tilde{J} \, \mathrm{d}\tilde{V}$$
$$+ \int_{\tilde{\Omega}_\mathrm{S}} \left(\rho_0^\mathrm{S} \frac{\partial \tilde{v}_i}{\partial t} \delta\tilde{v}_i + P_{ki} \delta\tilde{v}_{i,k} - \rho_0^\mathrm{S} f_i \delta\tilde{v}_i \right) \mathrm{d}\tilde{V}$$
$$- \int_{\tilde{\Gamma}_{\mathrm{F,N,v}}} \tilde{t}_i^\mathrm{F} \delta\tilde{v}_i \, \mathrm{d}\tilde{A} - \int_{\tilde{\Gamma}_{\mathrm{S,N,v}}} \tilde{t}_i^\mathrm{S} \delta\tilde{v}_i \, \mathrm{d}\tilde{A}$$
$$+ \int_{\tilde{\Omega}_\mathrm{F}} \alpha^\mathrm{disp} \tilde{u}_{i,j} \delta\tilde{u}_{i,j} \, \mathrm{d}\tilde{V} + \int_{\tilde{\Omega}_\mathrm{S}} \frac{\rho^\mathrm{F}}{(\Delta t)^2} \left(\frac{\partial \tilde{u}_i}{\partial t} - \tilde{v}_i \right) \delta\tilde{u}_i \, \mathrm{d}\tilde{V} = 0. \tag{4.36}$$

Note that the two boundary integrals on the interface Γ_I^x eliminate each

other since we demand that

$$
\begin{aligned}
&-\int_{\Gamma_{\mathrm{I}}^x} t_i^{\mathrm{S}} \delta\tilde{v}_i \,\mathrm{d}a = -\int_{\Gamma_{\mathrm{I}}^x} \sigma_{ji}^{\mathrm{S}} n_j^{\mathrm{S}} \delta\tilde{v}_i \,\mathrm{d}a = \int_{\Gamma_{\mathrm{I}}^x} \sigma_{ji}^{\mathrm{F}} n_j^{\mathrm{F}} \delta\tilde{v}_i \,\mathrm{d}a = \int_{\Gamma_{\mathrm{I}}^x} t_i^{\mathrm{F}} \delta\tilde{v}_i \,\mathrm{d}a \\
&\Rightarrow -\int_{\Gamma_{\mathrm{I}}^x} t_i^{\mathrm{F}} \delta\tilde{v}_i \,\mathrm{d}a - \int_{\Gamma_{\mathrm{I}}^x} t_i^{\mathrm{S}} \delta\tilde{v}_i \,\mathrm{d}a = 0. \qquad (4.37)
\end{aligned}
$$

Consequently, the second interaction condition, the equilibrium of forces, is already fulfilled in the above weak form, Eq. (4.36).

4.2 Discretization and solution technique

For the temporal discretization of all time derivatives in the overall weak form given in Eq. (4.36), the backward EULER scheme is employed as introduced in Eq. (3.25).

Spatial discretization is realized by means of the FEM. The trial and test function spaces are spanned by linear, continuous basis functions for the pressure variable $\tilde{p}$ and quadratic, continuous basis functions for the velocity $\tilde{v}_i$ and the displacement $\tilde{u}_i$. This discretization differs from the one proposed in [16] where biquadratic elements (continuous, 9 nodes on a quadrilateral) are used for the velocity and the displacement in combination with linear, discontinuous elements for the pressure. The choice of quadratic, continuous elements for the velocity and linear, continuous elements for the pressure is motivated by the fulfillment of the so called LADYZHENSKAYA–BABUSKA–BREZZI condition (LBB condition, [5]) which ensures the stability of the solution in the case of an isothermal and incompressible flow problem. The latter element pair[2] is extended by quadratic, continuous elements for the displacement within the monolithic solution method introduced in this thesis.

The weak form is solved using the NEWTON–RAPHSON method. The resulting systems of linear equations are solved by the direct solver MUMPS [24]. Since the matrix of the linear system is ill-conditioned and unsymmetric, iterative solution approaches with KRYLOV subspace methods like the generalized minimal residual (GMRES) solver, only work with good preconditioners [35, p. 87]. For the development of such preconditioners and other iterative solution approaches, we refer to [35] and the references cited therein. As long as the number of unknowns does not exceed a certain limit, a direct solver is assessed to be an appropriate choice as linear solver.

[2] This element pair belongs to the so called TAYLOR–HOOD family [29].

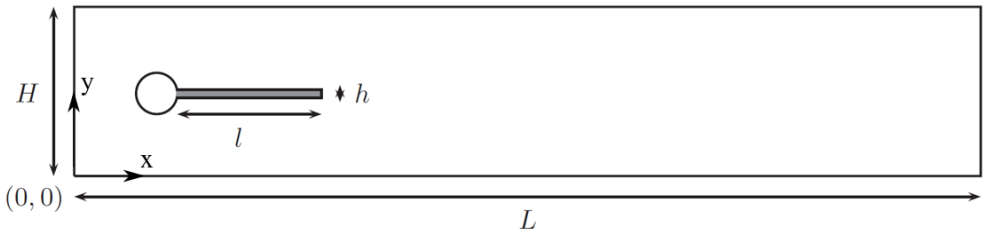

Fig. 4.1: Computational domain [31]

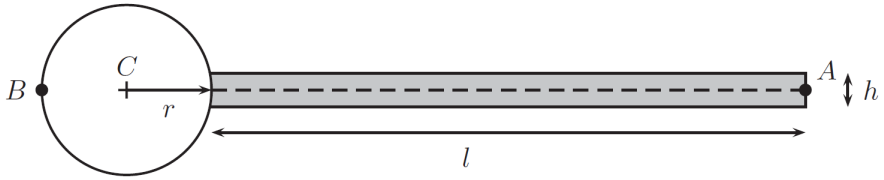

Fig. 4.2: Rigid obstacle (circle) and elastic structure [31]

4.3 Validation

In order to validate the developed monolithic solution method, it is applied to a benchmark setting which is quite popular in the FSI community. It is described in [31] and provides a complete problem definition including a geometry, initial and boundary conditions, material data and numerically computed results as reference data. It is used by many scientists for comparison of results and validation of different solution approaches; see, for example, [32].

The computational domain is illustrated in Fig. 4.1. It basically constitutes a channel with an inlet on the left and an outlet on the right. A rigid obstacle (circle) is placed intentionally not exactly at half of the channel height. An elastic bar is attached to the rigid body. The two structures are shown in detail in Fig. 4.2. The geometry is completely prescribed. While the fluid is assumed to be incompressible and described by the Navier–Stokes's constitutive equation, the structure is compressible and modeled by the St. Venant–Kirchhoff constitutive relation. The interface conditions—the continuity of velocities and the equilibrium of forces at the interface—are considered in the weak formulation of the FSI problem. A velocity is prescribed at the inlet and a *do nothing* boundary condition[3] is proposed for the outlet. On all remaining

[3]Unlike the *zero shear stress* boundary condition applied in Sect. 3.1, the boundary integral of the complete traction vector, t_i, is neglected for a *do nothing* boundary condition.

boundaries *no-slip* boundary conditions are applied for the velocity. Material parameters and inflow velocity are chosen according to the FSI2 setup [31, Tab. 12]. In order to quantify the FSI, the displacement of the reference point A in Fig. 4.2 is recorded.

Before the weak form in Eq. (4.36) can be applied to the FSI problem, the actual numerical values of the mesh motion coefficient α^{disp} and the artificial pressure coefficient α^{pres} have to be determined. Since both coefficients generally have to be small, they are specified as follows:

$$\alpha^{\text{disp}} = \frac{\varepsilon}{(\beta R)^{\gamma}}, \qquad \alpha^{\text{pres}} = \varepsilon, \tag{4.38}$$

where ε is a small number which has to be determined by means of a convergence analysis. Local stiffening is desired around the reference point A in Fig. 4.2. Hence, R describes the distance to this point. Furthermore, the distance is scaled by

$$\beta = \frac{1}{\delta}, \tag{4.39}$$

where δ is a radius around the reference point A within the stiffness is supposed to increase. A reasonable choice for δ is approximately one half of the distance of point A to the nearest wall where the fluid mesh motion becomes zero. The parameter γ can be set to $\gamma = 0$ at the beginning which is equivalent to a constant mesh motion coefficient $\alpha^{\text{disp}} = \varepsilon$. If the mesh quality is poor around the point A, γ can be increased causing enhanced local stiffening in the area inside δ and higher resilience outside of δ. Note that, in general, the choice of the mesh motion coefficient α^{disp} heavily depends on the specific problem. The effects of different parameters of the chosen α^{disp} are illustrated in Fig. 4.3. The illustrated mesh deformations range from inadmissible element distortions (a, b) to a relatively uniform mesh deformation (e, f).

Although the element quality in Fig. 4.3 (f) seems to suffice, numerical problems have been observed around the corners of the bar even for higher values of γ. In order to stiffen the fluid mesh around these corners, the mesh motion coefficient in Eq. (4.38) has been improved and replaced by

$$\alpha^{\text{disp}} = \frac{\varepsilon}{\left(\left(\beta R^{\text{a}}\right)\left(\beta R^{\text{b}}\right)\right)^{\gamma}}, \tag{4.40}$$

where R^{a} and R^{b} are the distances to the corners above and below the reference point A.

Consequently, the following three steps have to be performed in order to ensure the convergence of the computed solution:

1. Decrease ε until a convergence of results is achieved. Increase γ for better mesh quality, if necessary.

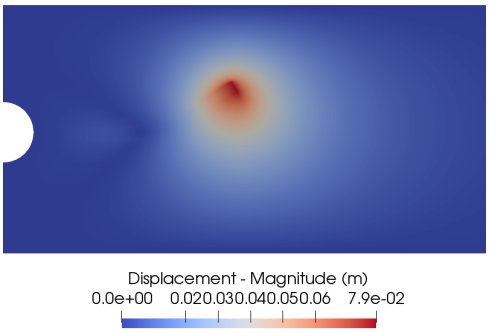

(a) Displacement field in spatial coordinates for $\varepsilon = \text{const.}$, $\gamma = 0$

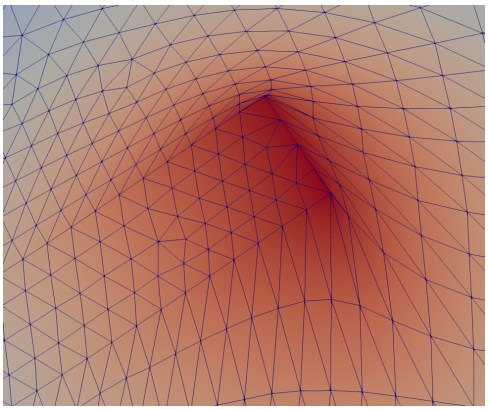

(b) Mesh deformation at reference point A for $\varepsilon = \text{const.}$, $\gamma = 0$

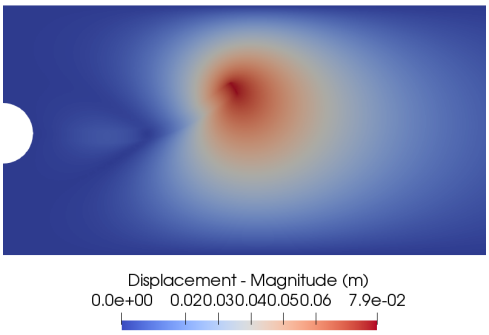

(c) Displacement field in spatial coordinates for $\varepsilon = \text{const.}$, $\beta = 10$, $\gamma = 1$

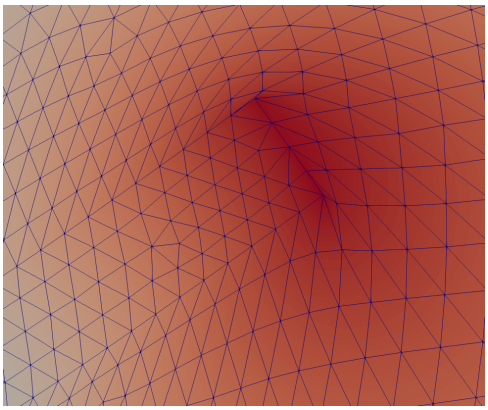

(d) Mesh deformation at reference point A for $\varepsilon = \text{const.}$, $\beta = 10$, $\gamma = 1$

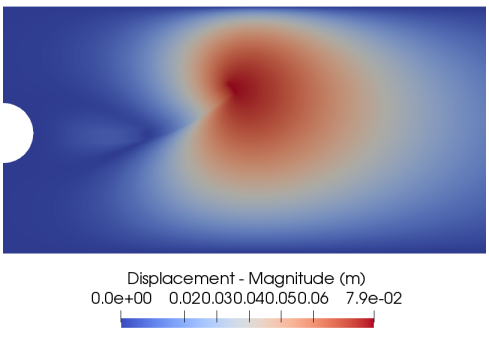

(e) Displacement field in spatial coordinates for $\varepsilon = \text{const.}$, $\beta = 10$, $\gamma = 2$

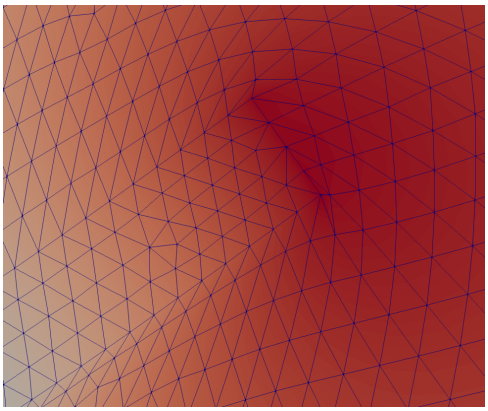

(f) Mesh deformation at reference point A for $\varepsilon = \text{const.}$, $\beta = 10$, $\gamma = 2$

Fig. 4.3: Different mesh motion coefficients and their impact on fluid mesh deformation

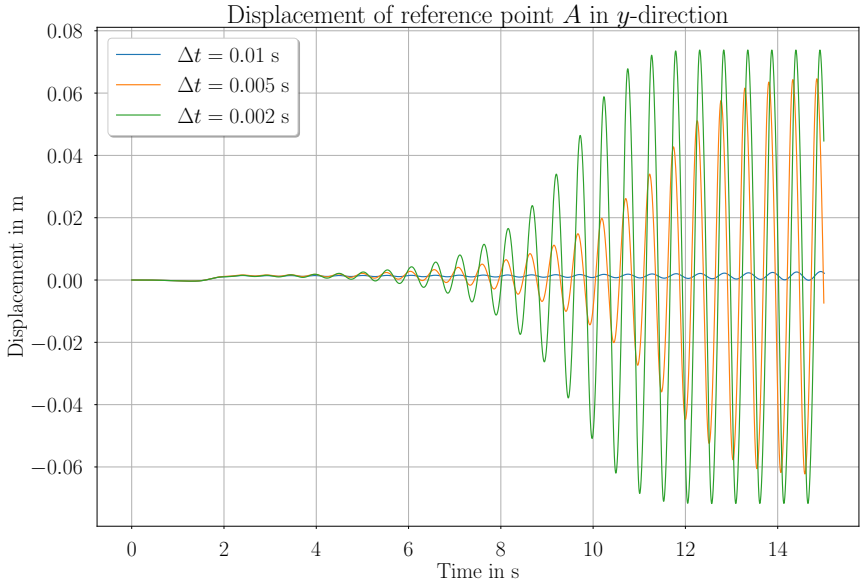

Fig. 4.4: Influence of different time step sizes Δt on the FSI regarding the displacement in y-direction of the reference point A

2. Refine the temporal discretization by selecting smaller time step sizes Δt.

3. Improve the spatial discretization by mesh refinement.

Due to the fact that the parameters in all three steps are independent of each other, the order of the convergence analysis is arbitrary. For the mesh motion coefficient in Eq. (4.40) and the artificial pressure coefficient in Eq. (4.38) the following parameters have been determined:

$$\delta = 0.05 \Rightarrow \beta = 20, \qquad \gamma = 1, \qquad \varepsilon = 10^{-20}. \tag{4.41}$$

The temporal discretization has a huge impact on the results. In Fig. 4.4 the displacement of the reference point A in the y-direction is presented for different time step sizes Δt; we abbreviate this displacement by u_y^{A} and the corresponding displacement in x-direction by u_x^{A}. The plot shows that the elastic structure oscillates as an outcome of the FSI. The oscillation enhances for smaller Δt. If Δt is too large, almost no oscillation occurs. A convergence analysis in time was performed by recording the maximum u_y^{A} within the time period $[0\,\mathrm{s}, 15\,\mathrm{s}]$. The results are summarized in Table 4.1. For the time convergence

Table 4.1: Comparison of different time step sizes, Δt, and the computation time of a simulation solved by 6 CPUs for the time period $[0\,\mathrm{s}, 15\,\mathrm{s}]$ with the computed maximum displacement of reference point A in y-direction, u_y^{A}, for a coarse mesh with 5468 vertices

Δt (s)	Comp. time (h)	Max. u_y^{A} (mm)
0.01	2	2.72
0.005	4	61.29
0.002	7	73.83
0.001	12	77.79
0.0005	22	79.75
0.0002	57	80.82
0.0001	132	81.20

Table 4.2: Comparison of different mesh refinement levels, numbers of (triangle) vertices of the triangulated mesh, degrees of freedom (DOF) of the linear system and the computation time of a simulation solved by 6 CPUs for the time period $[0\,\mathrm{s}, 15\,\mathrm{s}]$ with the computed maximum displacement of reference point A in y-direction, u_y^{A}, for $\Delta t = 0.005\,\mathrm{s}$

Ref. level	Vertices	DOF	Comp. time (h)	Max. u_y^{A} (mm)
1	5468	91304	4	61.29
2	17904	301276	16	64.60
3	33464	564756	24	64.67
4	53896	911252	50	64.73

analysis and the plot in Fig. 4.4 a very coarse mesh with 5468 vertices was utilized and the problem was solved by 6 central processing units (CPUs, "Intel Xeon Broadwell-EX series E7-4850") run in parallel. As a compromise between accuracy and computation time, the time step size $\Delta t = 0.0002\,\mathrm{s}$ was selected for the validation of the monolithic approach.

The spatial convergence analysis is summarized in Table 4.2. Several mesh refinement levels leading to increased degrees of freedom (DOF) of the discretized system were examined using a time step size of $\Delta t = 0.005\,\mathrm{s}$. As for the temporal convergence analysis, the problem was solved by 6 CPUs run in parallel. Refinement level 2 suffices with regard to the accuracy of the time discretization and is, therefore, selected for the validation.

The validation is accomplished by comparing the results of a computation involving the determined parameters with the reference data provided by [30].

In Fig. 4.5 both computed and reference data are plotted. In both directions the amplitudes of the oscillations are nearly equal. However, a small phase shift can be identified between the two oscillations. One possible explanation for the phase shift is the use of different mesh motion models [14, p. 43]. In general, the computed solution agrees very well with the reference data.

Contour plots of the computed solution for the velocity and pressure fields are presented in Fig. 4.6 and Fig. 4.7 for a fixed time point in order to visualize the fluid dynamics of the benchmark problem.

4.4 Alternative approach with linear finite elements

In this section an alternative approach is introduced which allows to use linear finite elements, i.e., solely linear, continuous basis functions span the trial and test spaces of the FEM. We abbreviate this approach by "P1P1P1" and the original method from Sect. 4.2 by "P2P2P1" with regard to the trial and test functions. The advantage of the "P1P1P1" method is that all computed field quantities ($\tilde{v}_i$, $\tilde{u}_i$, $\tilde{p}$) are discretized equally such that a coupling to other field quantities like temperature or mass density might be easier to realize.

Since we fail to solve the weak form in Eq. (4.36) with linear elements, we incorporate the method introduced in [1] for the computation of the fluid flow with linear elements. We basically exploit the balance of linear momentum a second time and begin with Eq. (4.5) for an ALE viewpoint,

$$\rho^{\mathrm{F}} \left.\frac{\partial v_i}{\partial t}\right|_{\boldsymbol{\chi}} + \rho^{\mathrm{F}} \left(v_j - w_j\right) \frac{\partial v_i}{\partial x_j} + \frac{\partial p}{\partial x_i} - \mu^{\mathrm{F}} \frac{\partial^2 v_i}{\partial x_j \partial x_j} - \mu^{\mathrm{F}} \frac{\partial^2 v_j}{\partial x_i \partial x_j} - \rho^{\mathrm{F}} f_i = 0. \tag{4.42}$$

Unlike the procedure in Sect. 4.1, Eq. (4.42) is multiplied by the gradient of the test function for the pressure $\delta\tilde{p}$ and integrated over the fluid subdomain in spatial coordinates which yields

$$\begin{aligned} \int_{\Omega_{\mathrm{F}}^x} \Bigg(& \rho^{\mathrm{F}} \left.\frac{\partial v_i}{\partial t}\right|_{\boldsymbol{\chi}} + \rho^{\mathrm{F}} \left(v_j - w_j\right) \frac{\partial v_i}{\partial x_j} - \rho^{\mathrm{F}} f_i \\ & + \frac{\partial p}{\partial x_i} - \mu^{\mathrm{F}} \frac{\partial^2 v_i}{\partial x_j \partial x_j} - \mu^{\mathrm{F}} \frac{\partial^2 v_j}{\partial x_i \partial x_j} \Bigg) \frac{\partial \delta\tilde{p}}{\partial x_i} \, \mathrm{d}v = 0. \end{aligned} \tag{4.43}$$

Without any partial integration the integral form is transformed into referential coordinates by applying the transformation rules given in Eq. (2.11)-Eq. (2.12)

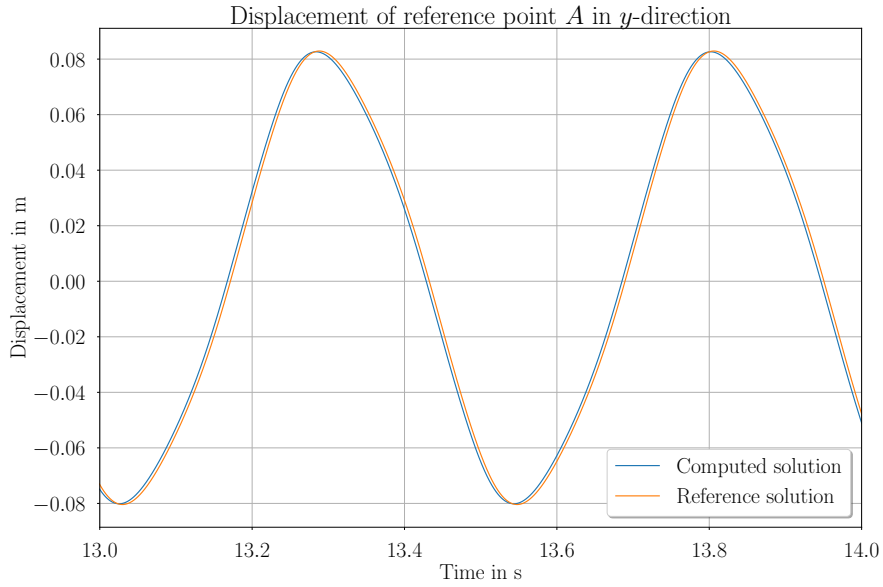

(a) in y-direction

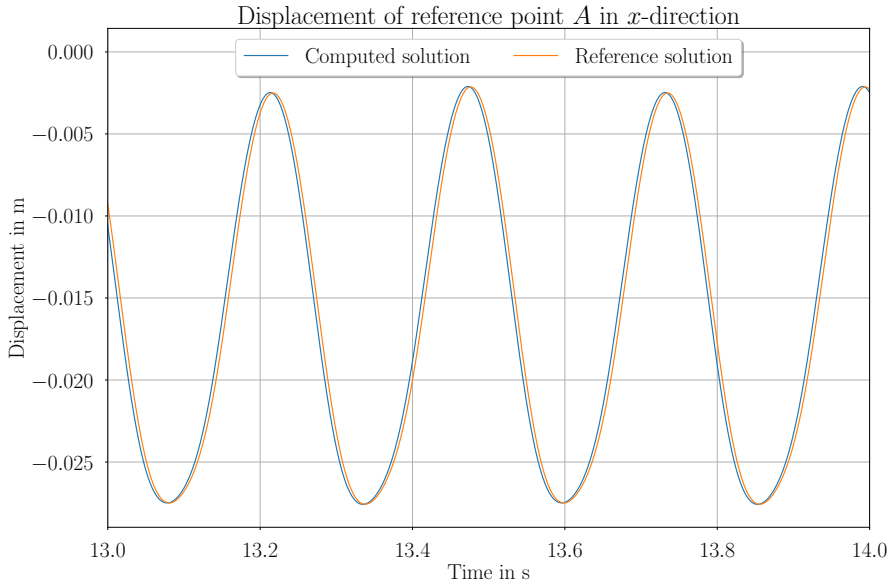

(b) in x-direction

Fig. 4.5: Comparison of the computed displacement of reference point A with reference data [30]; computation time: 239 h

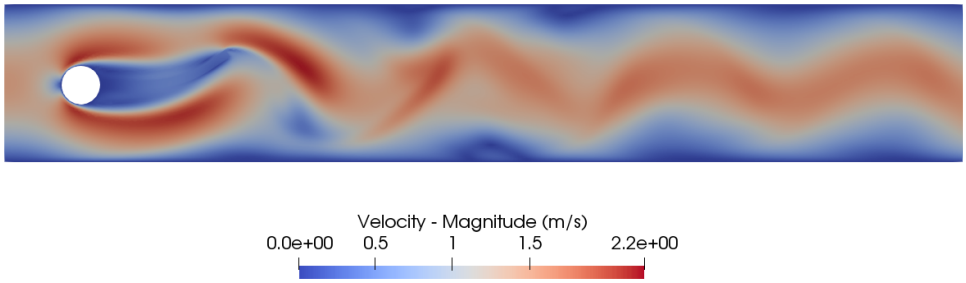

(a) in the whole domain

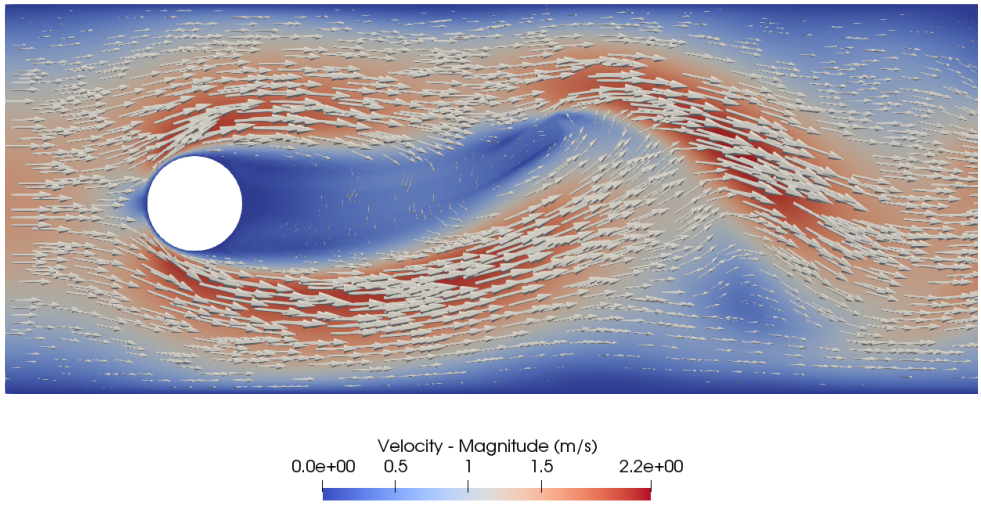

(b) around the elastic structure

Fig. 4.6: Computed velocity field at $t = 13.28\,\mathrm{s}$

such that we obtain

$$\int_{\Omega_{\mathrm{F}}^{\chi}} \left(\rho^{\mathrm{F}} \left. \frac{\partial v_i}{\partial t} \right|_{\boldsymbol{\chi}} + \rho^{\mathrm{F}} \left(v_j - w_j \right) \frac{\partial v_i}{\partial \chi_k} \left(\hat{\boldsymbol{F}}^{-1} \right)_{kj} - \rho^{\mathrm{F}} f_i + \frac{\partial p}{\partial \chi_k} \left(\hat{\boldsymbol{F}}^{-1} \right)_{ki} \right.$$
$$\left. - \mu^{\mathrm{F}} \frac{\partial}{\partial \chi_k} \left(\hat{\boldsymbol{F}}^{-1} \right)_{kj} \left(\frac{\partial v_i}{\partial \chi_l} \left(\hat{\boldsymbol{F}}^{-1} \right)_{lj} + \frac{\partial v_j}{\partial \chi_l} \left(\hat{\boldsymbol{F}}^{-1} \right)_{li} \right) \right) \frac{\partial \delta \tilde{p}}{\partial \chi_m} \left(\hat{\boldsymbol{F}}^{-1} \right)_{mi} \hat{J} \, \mathrm{d}\hat{V} = 0. \tag{4.44}$$

Equation (4.44) is rewritten in the notation for the monolithic problem and converted into the unit of power by multiplying with Δt and dividing by ρ^{F}

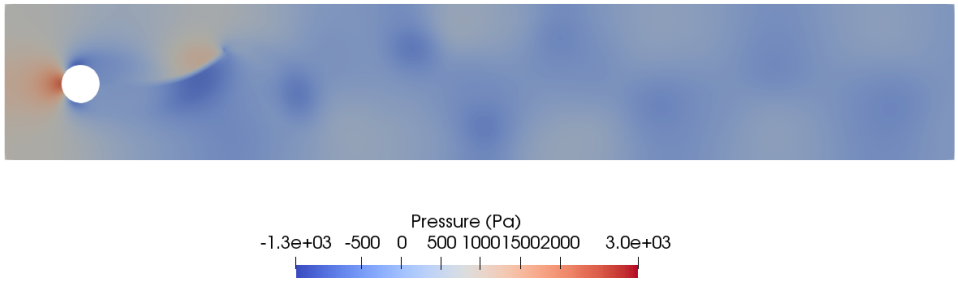

(a) in the whole domain

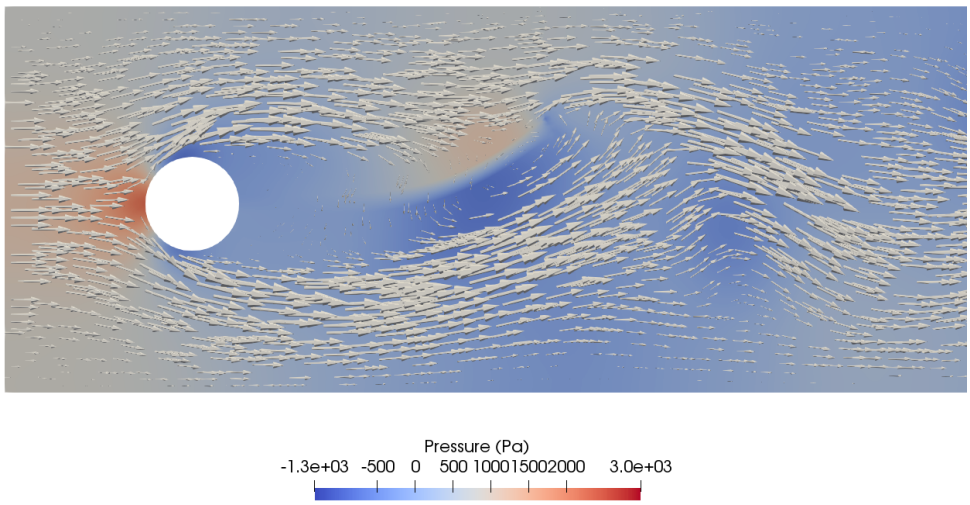

(b) around the elastic structure

Fig. 4.7: Computed pressure field and velocity vectors as arrows at $t = 13.28\,\mathrm{s}$

such that it can be added to the original weak form for the overall FSI problem, Eq. (4.36). The resulting weak form reads

$$
\begin{aligned}
&\int_{\tilde{\Omega}_\mathrm{F}} \tilde{v}_{i,k} \left(\tilde{\boldsymbol{F}}^{-1}\right)_{ki} \delta\tilde{p}\tilde{J}\,\mathrm{d}\tilde{V} + \int_{\tilde{\Omega}_\mathrm{S}} \alpha^{\mathrm{pres}} \tilde{p}_{,j}\delta\tilde{p}_{,j}\,\mathrm{d}\tilde{V} \\
&+ \int_{\tilde{\Omega}_\mathrm{F}} \frac{\Delta t}{\rho^\mathrm{F}} \Bigg(\rho^\mathrm{F} \frac{\partial \tilde{v}_i}{\partial t} + \rho^\mathrm{F} \left(\tilde{v}_j - \frac{\partial \tilde{u}_j}{\partial t}\right) \tilde{v}_{i,k} \left(\tilde{\boldsymbol{F}}^{-1}\right)_{kj} - \rho^\mathrm{F} f_i + \tilde{p}_{,k} \left(\tilde{\boldsymbol{F}}^{-1}\right)_{ki} \\
&- \mu^\mathrm{F} \Bigg(\tilde{v}_{i,l} \left(\tilde{\boldsymbol{F}}^{-1}\right)_{lj} + \tilde{v}_{j,l} \left(\tilde{\boldsymbol{F}}^{-1}\right)_{li} \Bigg)_{,k} \left(\tilde{\boldsymbol{F}}^{-1}\right)_{kj} \Bigg) \delta\tilde{p}_{,m} \left(\tilde{\boldsymbol{F}}^{-1}\right)_{mi} \tilde{J}\,\mathrm{d}\tilde{V} \\
&+ \int_{\tilde{\Omega}_\mathrm{F}} \Bigg(\Bigg(\rho^\mathrm{F} \frac{\partial \tilde{v}_i}{\partial t} + \rho^\mathrm{F} \left(\tilde{v}_j - \frac{\partial \tilde{u}_j}{\partial t}\right) \tilde{v}_{i,k} \left(\tilde{\boldsymbol{F}}^{-1}\right)_{kj} - \rho^\mathrm{F} f_i \Bigg) \delta\tilde{v}_i - \tilde{p}\delta\tilde{v}_{i,k} \left(\tilde{\boldsymbol{F}}^{-1}\right)_{ki} \\
&+ \mu^\mathrm{F} \left(\tilde{v}_{i,k} \left(\tilde{\boldsymbol{F}}^{-1}\right)_{kj} + \tilde{v}_{j,k} \left(\tilde{\boldsymbol{F}}^{-1}\right)_{ki} \right) \delta\tilde{v}_{i,l} \left(\tilde{\boldsymbol{F}}^{-1}\right)_{lj} \Bigg) \tilde{J}\,\mathrm{d}\tilde{V} \\
&+ \int_{\tilde{\Omega}_\mathrm{S}} \left(\rho_0^\mathrm{S} \frac{\partial \tilde{v}_i}{\partial t} \delta\tilde{v}_i + P_{ki}\delta\tilde{v}_{i,k} - \rho_0^\mathrm{S} f_i \delta\tilde{v}_i \right) \mathrm{d}\tilde{V} \\
&- \int_{\tilde{\Gamma}_{\mathrm{F,N,v}}} \tilde{t}_i^\mathrm{F} \delta\tilde{v}_i\,\mathrm{d}\tilde{A} - \int_{\tilde{\Gamma}_{\mathrm{S,N,v}}} \tilde{t}_i^\mathrm{S} \delta\tilde{v}_i\,\mathrm{d}\tilde{A} \\
&+ \int_{\tilde{\Omega}_\mathrm{F}} \alpha^{\mathrm{disp}} \tilde{u}_{i,j}\delta\tilde{u}_{i,j}\,\mathrm{d}\tilde{V} + \int_{\tilde{\Omega}_\mathrm{S}} \frac{\rho^\mathrm{F}}{(\Delta t)^2} \left(\frac{\partial \tilde{u}_i}{\partial t} - \tilde{v}_i \right) \delta\tilde{u}_i\,\mathrm{d}\tilde{V} = 0. \qquad (4.45)
\end{aligned}
$$

By means of the alternative weak form in Eq. (4.45) and linear elements the FSI problem can be computed without further modifications. The results of a convergence analysis in space for the benchmark problem are shown in Table 4.3; see Sect. 4.3 and Table 4.2 for a detailed description of the compared quantities. Mesh refinement level 4 is expected to be the most appropriate

Table 4.3: Spatial convergence analysis for alternative approach with linear elements for $\Delta t = 0.0002\,\mathrm{s}$

Ref. level	Vertices	DOF	Comp. time (h)	Max. u_y^A (mm)
2	17904	89520	47	74.95
3	33464	167320	118	79.95
4	53896	269480	180	81.59

discretization for comparison with the original algorithm (P2P2P1) due to a similar number of degrees of freedom (DOF). The results of the two developed solution methods and the reference solution are plotted in Fig. 4.8. Both

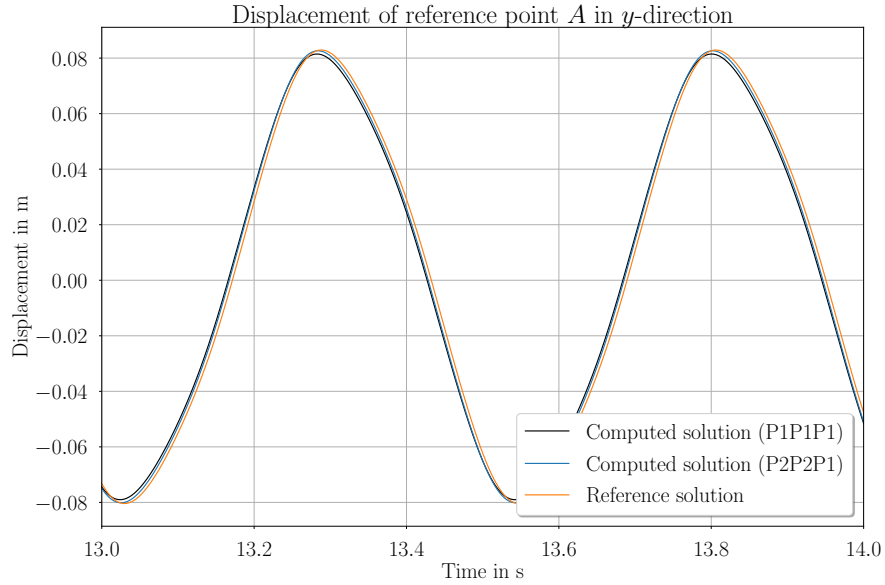

(a) in y-direction

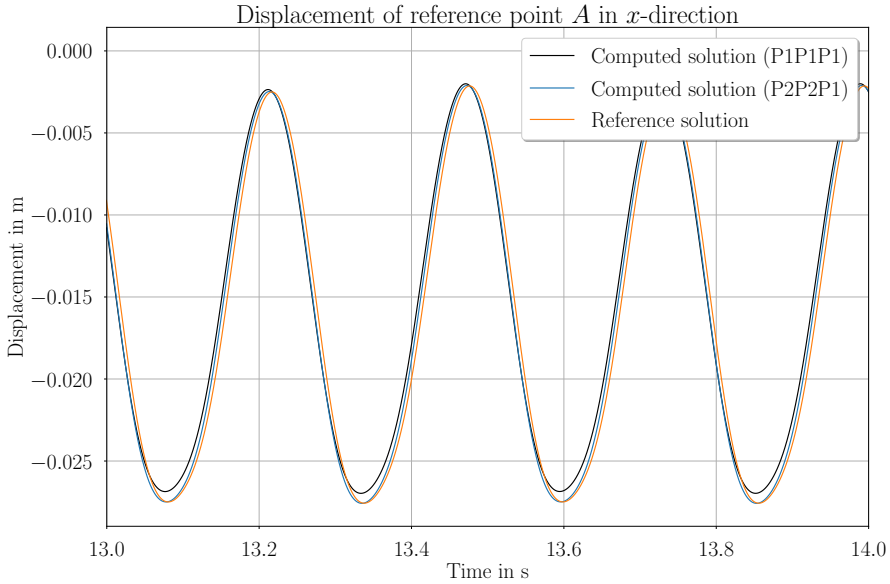

(b) in x-direction

Fig. 4.8: Comparison of the computed displacement of reference point A using linear elements (P1P1P1, refinement level 4) with the original solution according to the previous sections (P2P2P1) and reference data [30]

computed solutions are in phase with each other. Yet, a small amplitude deviation can be observed. In general, a relatively good match of the computed solutions and the reference solution is achieved. Therefore, both solution methods constitute valid approaches for the simulation of FSI problems.

5 Extension to thermomechanical fluid–structure interaction

In the following chapter a monolithic computational approach for thermomechanical FSI is presented. The fluid is assumed to be incompressible and modeled by the Navier–Stokes–Fourier constitutive equations, while the structure is compressible and described by a linear thermoelastic material model.

Research on solution approaches for thermomechanical FSI, sometimes called thermal fluid–structure interaction (TFSI), can be rarely found in the literature [38]. Nevertheless, the inclusion of temperature effects in FSI problems is reasonable and sometimes even mandatory. Especially, in the fields of turbo machinery and heat exchangers, FSI has to be computed with regard to mechanical and thermal quantities; see, for example, [12]. One monolithic solution procedure for thermomechanical FSI, which basically follows the same idea as the one in this thesis, has been developed by [38]. Further publications related to the topic of thermomechanical FSI can be found in [8], [10], [25].

First, the weak form for the thermomechanical FSI problem is introduced. The problem is solved numerically by extending the FEM from Sect. 4.4 with linear elements in order to include the temperature field. Finally, computed solutions of the extended benchmark problem from Sect. 4.3 are presented with the intent to validate the solution method qualitatively. The computations are conducted using the FEniCS computing platform [3].

5.1 Weak form

The weak form can be generated analogously to the procedure introduced in Sect. 4.1. In contrast to the mechanical FSI problem, the balance of entropy is additionally evaluated for the thermomechanical FSI problem in order to compute the temperature. Besides, the constitutive equations of a Navier–Stokes–Fourier fluid and a linear thermoelastic solid are utilized; see Sect. 2.3.3 and Sect. 2.3.4. The resulting equations for the thermal and mechanical field quantities are coupled in the whole domain.

5.1.1 Weak form in the fluid subdomain

For the weak form in the fluid subdomain, we begin with the balance of entropy in EULERian form, Eq. (2.30), and introduce the ALE viewpoint by Eq. (2.19):

$$\begin{aligned} &\rho^{\mathrm{F}} \left(\left. \frac{\partial \eta}{\partial t} \right|_{\boldsymbol{x}} + v_i \frac{\partial \eta}{\partial x_i} \right) + \frac{\partial}{\partial x_i} \left(\frac{q_i}{T} \right) - \rho^{\mathrm{F}} \frac{r}{T} = \frac{1}{T} \, {}^{\mathrm{d}}\sigma_{ij} \frac{\partial v_j}{\partial x_i} - \frac{q_i}{T^2} \frac{\partial T}{\partial x_i} \\ \Leftrightarrow \; &\rho^{\mathrm{F}} \left(\left. \frac{\partial \eta}{\partial t} \right|_{\boldsymbol{\chi}} + (v_i - w_i) \frac{\partial \eta}{\partial x_i} \right) + \frac{\partial}{\partial x_i} \left(\frac{q_i}{T} \right) - \rho^{\mathrm{F}} \frac{r}{T} = \frac{1}{T} \, {}^{\mathrm{d}}\sigma_{ij} \frac{\partial v_j}{\partial x_i} - \frac{q_i}{T^2} \frac{\partial T}{\partial x_i}. \end{aligned} \tag{5.1}$$

The integral form is attained in spatial coordinates by eliminating the right-hand side of Eq. (5.1), multiplying with $\delta\tilde{T}$ and integrating over the fluid subdomain:

$$\begin{aligned} \int_{\Omega_{\mathrm{F}}^x} \Bigg(&\rho^{\mathrm{F}} \left(\left. \frac{\partial \eta}{\partial t} \right|_{\boldsymbol{\chi}} + (v_i - w_i) \frac{\partial \eta}{\partial x_i} \right) + \frac{\partial}{\partial x_i} \left(\frac{q_i}{T} \right) \\ &- \rho^{\mathrm{F}} \frac{r}{T} + \frac{q_i}{T^2} \frac{\partial T}{\partial x_i} - \frac{1}{T} \, {}^{\mathrm{d}}\sigma_{ij} \frac{\partial v_j}{\partial x_i} \Bigg) \delta\tilde{T} \, \mathrm{d}v = 0. \end{aligned} \tag{5.2}$$

Partial integration of the flux term leads to

$$\begin{aligned} \int_{\Omega_{\mathrm{F}}^x} \Bigg(&\rho^{\mathrm{F}} \left(\left. \frac{\partial \eta}{\partial t} \right|_{\boldsymbol{\chi}} + (v_i - w_i) \frac{\partial \eta}{\partial x_i} \right) \delta\tilde{T} - \frac{q_i}{T} \frac{\partial \delta\tilde{T}}{\partial x_i} \\ &- \rho^{\mathrm{F}} \frac{r}{T} \delta\tilde{T} + \frac{q_i}{T^2} \frac{\partial T}{\partial x_i} \delta\tilde{T} - \frac{\delta\tilde{T}}{T} \, {}^{\mathrm{d}}\sigma_{ij} \frac{\partial v_j}{\partial x_i} \Bigg) \mathrm{d}v \\ &+ \int_{\Gamma_{\mathrm{F,N,T}}^x} \frac{q_i}{T} \delta\tilde{T} n_i^{\mathrm{F}} \, \mathrm{d}a + \int_{\Gamma_{\mathrm{I}}^x} \frac{q_i}{T} \delta\tilde{T} n_i^{\mathrm{F}} \, \mathrm{d}a = 0. \end{aligned} \tag{5.3}$$

Next, the constitutive relations given in Eq. (2.44) and Eq. (2.47) for q_i and ${}^{\mathrm{d}}\sigma_{ij}$ are plugged in and the balance of mass for an incompressible fluid, Eq. (3.4), is evaluated such that the divergence term in ${}^{\mathrm{d}}\sigma_{ij}$ vanishes. Then the first two integrals are transformed into referential coordinates by using the transformation

rules in Eq. (2.11)-Eq. (2.14) such that we obtain

$$\begin{aligned}
&\int_{\Omega_{\mathrm{F}}^{\chi}} \Bigg(\rho^{\mathrm{F}} \left(\left. \frac{\partial \eta}{\partial t} \right|_{\boldsymbol{\chi}} + (v_i - w_i) \frac{\partial \eta}{\partial \chi_k} \left(\hat{\boldsymbol{F}}^{-1} \right)_{ki} \right) \delta\tilde{T} - \rho^{\mathrm{F}} \frac{r}{T} \delta\tilde{T} \\
&+ \frac{\kappa^{\mathrm{F}}}{T} \frac{\partial T}{\partial \chi_k} \left(\hat{\boldsymbol{F}}^{-1} \right)_{ki} \frac{\partial \delta\tilde{T}}{\partial \chi_l} \left(\hat{\boldsymbol{F}}^{-1} \right)_{li} - \frac{\kappa^{\mathrm{F}}}{T^2} \frac{\partial T}{\partial \chi_k} \left(\hat{\boldsymbol{F}}^{-1} \right)_{ki} \frac{\partial T}{\partial \chi_l} \left(\hat{\boldsymbol{F}}^{-1} \right)_{li} \delta\tilde{T} \\
&- \frac{\delta\tilde{T}}{T} \frac{\partial v_j}{\partial \chi_k} \left(\hat{\boldsymbol{F}}^{-1} \right)_{ki} \mu^{\mathrm{F}} \left(\frac{\partial v_i}{\partial \chi_l} \left(\hat{\boldsymbol{F}}^{-1} \right)_{lj} + \frac{\partial v_j}{\partial \chi_l} \left(\hat{\boldsymbol{F}}^{-1} \right)_{li} \right) \Bigg) \hat{J} \, \mathrm{d}\hat{V} \\
&+ \int_{\Gamma_{\mathrm{F,N,T}}^{\chi}} \frac{\hat{q}^{\mathrm{F}}}{T} \delta\tilde{T} \, \mathrm{d}\hat{A} + \int_{\Gamma_{\mathrm{I}}^{x}} \frac{q^{\mathrm{F}}}{T} \delta\tilde{T} \, \mathrm{d}a = 0.
\end{aligned} \tag{5.4}$$

Here $q^{\mathrm{F}} = q_i^{\mathrm{F}} n_i^{\mathrm{F}}$ denotes the heat flux in normal direction and spatial coordinates while $\hat{q}^{\mathrm{F}}$ is the normal heat flux in referential coordinates such that

$$\begin{aligned}
&\int_{\Gamma_{\mathrm{F,N,T}}^{\chi}} \frac{\hat{q}^{\mathrm{F}}}{T} \delta\tilde{T} \, \mathrm{d}\hat{A} = \int_{\Gamma_{\mathrm{F,N,T}}^{\chi}} \frac{\hat{q}_i^{\mathrm{F}}}{T} \delta\tilde{T} \hat{J} \left(\hat{\boldsymbol{F}}^{-1} \right)_{li} \hat{N}_l^{\mathrm{F}} \, \mathrm{d}\hat{A} \\
&= - \int_{\Gamma_{\mathrm{F,N,T}}^{\chi}} \frac{\kappa^{\mathrm{F}}}{T} \frac{\partial T}{\partial \chi_k} \left(\hat{\boldsymbol{F}}^{-1} \right)_{ki} \delta\tilde{T} \hat{J} \left(\hat{\boldsymbol{F}}^{-1} \right)_{li} \hat{N}_l^{\mathrm{F}} \, \mathrm{d}\hat{A} = \int_{\Gamma_{\mathrm{F,N,T}}^{x}} \frac{q_i^{\mathrm{F}}}{T} \delta\tilde{T} n_i^{\mathrm{F}} \, \mathrm{d}a.
\end{aligned} \tag{5.5}$$

The boundary integral on the interface Γ_{I}^{x} is not transformed since it will be later applied for the thermal interaction condition of the equilibrium of normal heat fluxes along the interface in spatial coordinates.

5.1.2 Weak form in the structure subdomain

For the structure, we exploit the balance of entropy in LAGRANGEan form as in Eq. (2.39):

$$\rho_0^{\mathrm{S}} \left. \frac{\partial \eta}{\partial t} \right|_{\boldsymbol{X}} + \frac{\partial}{\partial X_i} \left(\frac{Q_i}{T} \right) - \rho_0^{\mathrm{S}} \frac{r}{T} = \frac{1}{T} \, {}^{\mathrm{d}} S_{ij} \left. \frac{\partial E_{ij}}{\partial t} \right|_{\boldsymbol{X}} - \frac{Q_i}{T^2} \frac{\partial T}{\partial X_i}. \tag{5.6}$$

The dissipative stress vanishes for a thermoelastic material; see Eq. (2.52). Therefore, Eq. (5.6) reduces to

$$\rho_0^{\mathrm{S}} \left. \frac{\partial \eta}{\partial t} \right|_{\boldsymbol{X}} + \frac{\partial}{\partial X_i} \left(\frac{Q_i}{T} \right) - \rho_0^{\mathrm{S}} \frac{r}{T} + \frac{Q_i}{T^2} \frac{\partial T}{\partial X_i} = 0. \tag{5.7}$$

The weak form of Eq. (5.7) is then given by

$$\int_{\Omega_{\mathrm{S}}^X} \left(\rho_0^{\mathrm{S}} \frac{\partial \eta}{\partial t}\bigg|_{\boldsymbol{X}} \delta\tilde{T} - \frac{Q_i}{T}\frac{\partial \delta\tilde{T}}{\partial X_i} - \rho_0^{\mathrm{S}}\frac{r}{T}\delta\tilde{T} + \frac{Q_i}{T^2}\frac{\partial T}{\partial X_i}\delta\tilde{T} \right) \mathrm{d}V + \int_{\Gamma_{\mathrm{S,N,T}}^X} \frac{\tilde{q}^{\mathrm{S}}}{T}\delta\tilde{T}\,\mathrm{d}A + \int_{\Gamma_{\mathrm{I}}^x} \frac{q^{\mathrm{S}}}{T}\delta\tilde{T}\,\mathrm{d}a = 0. \tag{5.8}$$

On the NEUMANN boundary $\Gamma_{\mathrm{S,N,T}}^X$, the normal heat flux $\tilde{q}^{\mathrm{S}} = Q_i^{\mathrm{S}} N_i^{\mathrm{S}}$ is written in material coordinates whereas the boundary integral on the interface Γ_{I}^x is formulated in spatial coordinates. With the definition of the heat flux in material coordinates, Eq. (2.35), and the transformation rule given in Eq. (2.13), the corresponding transformation reads

$$\begin{aligned} \int_{\Gamma_{\mathrm{I}}^X} \frac{Q_i^{\mathrm{S}}}{T}\delta\tilde{T} N_i^{\mathrm{S}}\,\mathrm{d}A &= \int_{\Gamma_{\mathrm{I}}^X} \frac{q_j^{\mathrm{S}}}{T}\delta\tilde{T}\left(\boldsymbol{F}^{-1}\right)_{ij} J N_i^{\mathrm{S}}\,\mathrm{d}A \\ &= \int_{\Gamma_{\mathrm{I}}^x} \frac{q_j^{\mathrm{S}}}{T}\delta\tilde{T} n_j^{\mathrm{S}}\,\mathrm{d}a = \int_{\Gamma_{\mathrm{I}}^x} \frac{q^{\mathrm{S}}}{T}\delta\tilde{T}\,\mathrm{d}a. \end{aligned} \tag{5.9}$$

5.1.3 Weak form in the whole domain

Let the left-hand side of the weak form in Eq. (4.45) be denoted by $\mathrm{Form}^{\mathrm{mech,P1P1P1}}$. Then the weak form for the thermomechanical, monolithic FSI problem is obtained by adding Eq. (5.4), Eq. (5.8) and $\mathrm{Form}^{\mathrm{mech,P1P1P1}}$ since all equations are given in the unit of power. In the notation for the monolithic problem with $\tilde{T} = T$, the weak form then reads

$$\begin{aligned} &\int_{\tilde{\Omega}_{\mathrm{F}}} \Bigg(\rho^{\mathrm{F}} \left(\frac{\partial \eta}{\partial t} + \left(\tilde{v}_i - \frac{\partial \tilde{u}_i}{\partial t} \right) \eta_{,k} \left(\tilde{\boldsymbol{F}}^{-1} \right)_{ki} \right) \delta\tilde{T} - \rho^{\mathrm{F}} \frac{r}{\tilde{T}}\delta\tilde{T} \\ &+ \frac{\kappa^{\mathrm{F}}}{\tilde{T}} \tilde{T}_{,k} \left(\tilde{\boldsymbol{F}}^{-1} \right)_{ki} \delta\tilde{T}_{,l} \left(\tilde{\boldsymbol{F}}^{-1} \right)_{li} - \frac{\kappa^{\mathrm{F}}}{\tilde{T}^2} \tilde{T}_{,k} \left(\tilde{\boldsymbol{F}}^{-1} \right)_{ki} \tilde{T}_{,l} \left(\tilde{\boldsymbol{F}}^{-1} \right)_{li} \delta\tilde{T} \\ &- \frac{\delta\tilde{T}}{\tilde{T}} \tilde{v}_{j,k} \left(\tilde{\boldsymbol{F}}^{-1} \right)_{ki} \mu^{\mathrm{F}} \left(\tilde{v}_{i,l} \left(\tilde{\boldsymbol{F}}^{-1} \right)_{lj} + \tilde{v}_{j,l} \left(\tilde{\boldsymbol{F}}^{-1} \right)_{li} \right) \Bigg) \tilde{J}\,\mathrm{d}\tilde{V} \\ &+ \int_{\tilde{\Omega}_{\mathrm{S}}} \left(\rho_0^{\mathrm{S}} \frac{\partial \eta}{\partial t}\delta\tilde{T} - \frac{Q_i}{\tilde{T}}\delta\tilde{T}_{,i} - \rho_0^{\mathrm{S}}\frac{r}{\tilde{T}}\delta\tilde{T} + \frac{Q_i}{\tilde{T}^2}\tilde{T}_{,i}\delta\tilde{T} \right) \mathrm{d}\tilde{V} \\ &+ \int_{\tilde{\Gamma}_{\mathrm{F,N,T}}} \frac{\tilde{q}^{\mathrm{F}}}{\tilde{T}}\delta\tilde{T}\,\mathrm{d}\tilde{A} + \int_{\tilde{\Gamma}_{\mathrm{S,N,T}}} \frac{\tilde{q}^{\mathrm{S}}}{\tilde{T}}\delta\tilde{T}\,\mathrm{d}\tilde{A} + \mathrm{Form}^{\mathrm{mech,P1P1P1}} = 0. \end{aligned} \tag{5.10}$$

Beside the equilibrium of forces, the obtained weak form in Eq. (5.10) also implies the equilibrium of heat fluxes along the interface as we have enforced that

$$\begin{aligned}
&\int_{\Gamma_{\mathrm{I}}^x} \frac{q^{\mathrm{S}}}{T} \delta\tilde{T} \,\mathrm{d}a = \int_{\Gamma_{\mathrm{I}}^x} \frac{q_i^{\mathrm{S}}}{T} \delta\tilde{T} n_i^{\mathrm{S}} \,\mathrm{d}a = -\int_{\Gamma_{\mathrm{I}}^x} \frac{q_i^{\mathrm{S}}}{T} \delta\tilde{T} n_i^{\mathrm{F}} \,\mathrm{d}a \\
&= -\int_{\Gamma_{\mathrm{I}}^x} \frac{q_i^{\mathrm{F}}}{T} \delta\tilde{T} n_i^{\mathrm{F}} \,\mathrm{d}a = -\int_{\Gamma_{\mathrm{I}}^x} \frac{q^{\mathrm{F}}}{T} \delta\tilde{T} \,\mathrm{d}a \\
&\Rightarrow \int_{\Gamma_{\mathrm{I}}^x} \frac{q^{\mathrm{S}}}{T} \delta\tilde{T} \,\mathrm{d}a + \int_{\Gamma_{\mathrm{I}}^x} \frac{q^{\mathrm{F}}}{T} \delta\tilde{T} \,\mathrm{d}a = 0. \qquad (5.11)
\end{aligned}$$

Alternatively, the mechanical FSI problem could be also formulated by the left-hand side of Eq. (4.36), i.e. $\mathrm{Form}^{\mathrm{mech,P2P2P1}}$ instead of $\mathrm{Form}^{\mathrm{mech,P1P1P1}}$, leading to another spatial discretization strategy.

5.2 Discretization and solution technique

The temporal discretization of the time derivatives in Eq. (5.10) is realized by means of the backward EULER scheme. For the spatial discretization we again employ an FEM in which both trial and test spaces are spanned by linear, continuous basis functions for each of the unknowns ($\tilde{p}$, $\tilde{v}_i$, $\tilde{u}_i$, $\tilde{T}$).

The use of continuous basis functions for the temperature $\tilde{T}$ ensures the continuity of the resulting temperature field. In particular, the temperature at the interface $\tilde{\Gamma}_{\mathrm{I}}$ is the same for both fluid and structure. This interaction condition can be easily justified and makes sense considering a *no-slip* interaction condition for the velocity. It can be further described as thermal equilibrium condition [38].

The weak form is solved using the NEWTON–RAPHSON method in combination with the direct solver MUMPS according to the argumentation presented in Sect. 4.2.

In case $\mathrm{Form}^{\mathrm{mech,P2P2P1}}$ is considered in Eq. (5.10), it is also possible to use quadratic, continuous ansatz functions for the velocity $\tilde{v}_i$ and the displacement $\tilde{u}_i$ and linear, continuous ansatz functions for the pressure $\tilde{p}$ and the temperature $\tilde{T}$. However, the first discretization strategy with solely linear elements is prefered in this thesis due to its simplicity and innovative quality and, therefore, used in the following section.

5.3 Results of the extended benchmark problem

In this section the developed method is verified as an appropriate solution procedure for thermomechanical FSI by its application to a modified version of the benchmark problem from Sect. 4.3 and a qualitative evaluation of the computed results.

The benchmark problem is extended to a thermomechanical FSI problem by additionally imposing a constant DIRICHLET boundary condition for the temperature $\tilde{T} = T^{\mathrm{amb}}$ at the inlet and setting the normal heat fluxes $\tilde{q}^{\mathrm{F}}$ and $\tilde{q}^{\mathrm{S}}$ to zero on the NEUMANN boundaries $\tilde{\Gamma}_{\mathrm{F,N,T}}$ and $\tilde{\Gamma}_{\mathrm{S,N,T}}$. The latter boundary condition is also called adiabatic boundary condition and can be interpreted as a perfectly insulated wall. The ambient temperature T^{amb} is adopted as initial condition in the whole domain. Further, a constant internal heating within the structure is prescribed by $r = r^{\mathrm{S}}$ while the internal heating is neglected in the fluid subdomain. The prescribed quantities are summarized with the chosen additional material parameters in Table 5.1.

Table 5.1: Prescribed quantities for thermomechanically extended benchmark problem

Parameter	Value
T^{amb} (K)	293.15
r^{S} (W/kg)	2500
c^{F} (J/(kg K))	24.28
κ^{F} (W/(m K))	28
c^{S} (J/(kg K))	1700
κ^{S} (W/(m K))	0.22
α^{S} (1/K)	0.00015

Since no quantitative data for comparison is available, the main focus lies on a qualitative evaluation of the results. That is why a rigorous convergence analysis is skipped. Instead, the parameters that are vital for the convergence of the solution are determined as a compromise between computation time and expected quality of the solution:

- The parameters of the mesh motion and artificial pressure problems are chosen according to Eq. (4.41).
- The time step size $\Delta t = 0.005\,\mathrm{s}$ is selected; see Table 4.1 for comparison of different time step sizes for the mechanical FSI problem in Sect. 4.3.
- Mesh refinement level 2, i.e., a mesh with 17904 vertices is chosen; see Table 4.2 for comparison of different mesh refinement levels for the mechanical FSI problem in Sect. 4.3.

(a) $t = 5\,\mathrm{s}$

(b) $t = 10\,\mathrm{s}$

(c) $t = 15\,\mathrm{s}$

Fig. 5.1: Computed temperature fields at different times

The computed temperature fields at different time points are presented in Fig. 5.1. The temperature results indicate that the heat transfer within and between the two subdomains is considered adequately by the developed approach. The heat transfer around the thermoelastic structure is shown in more detail in Fig. 5.2. Beside the combined thermal and mechanical interaction between the fluid and the structure, it is emphasized that the

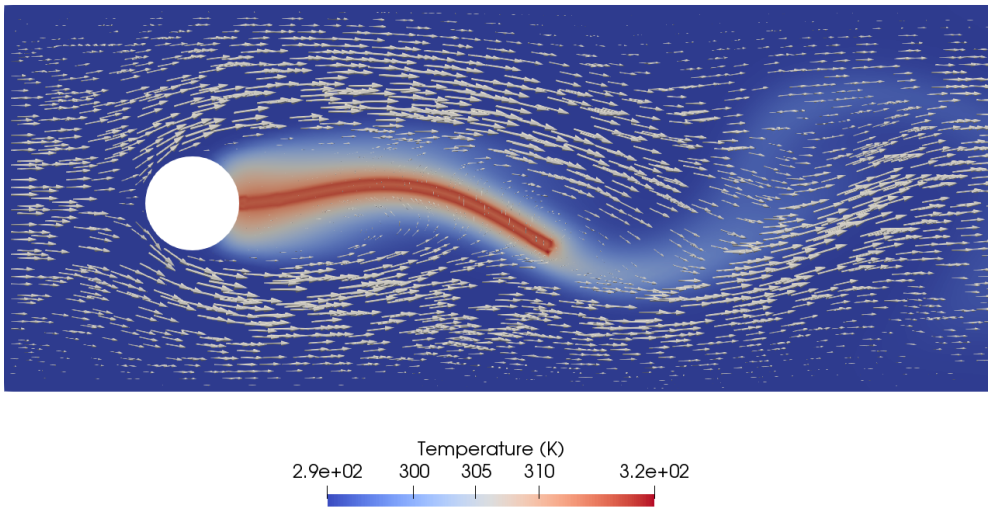

Fig. 5.2: Computed temperature field around the thermoelastic structure

developed algorithm also considers a thermomechanical coupling in each of the subdomains, i.e., the fluid velocity causes higher temperatures within the fluid and the structure temperature affects the displacement of the structure.

The material parameters in Table 5.1 are chosen such that a good visualization of the underlying physics is provided. The thermal parameters of the structure are adopted from polypropylene [26]. It should be noted that the use of values for c^{F} and κ^{F} which are close to those of glycerine causes numerical problems with the given mesh. These problems were observed especially in the left third of the channel, where high velocity gradients are computed, and can be avoided by means of a finer mesh. It is assumed that the observed errors in the temperature field stem from a computed velocity field which is locally not accurate enough in order to approximate the convective term in Eq. (5.4) sufficiently.

6 Summary and outlook

Fluid–structure interaction (FSI) is a phenomenon which is found in probably countless technical systems. Its computation helps to improve the efficiency, dependability and durability of highly sophisticated products.

In the course of this thesis, a monolithic computational approach for the FSI of an incompressible, viscous fluid with a compressible, linear elastic structure is developed based on the procedure in [16]. The developed method, however, differs in several aspects like the choice of equations in the weak form and the utilized discretization techniques due to

- the use of continuous basis functions within the FEM (P2P2P1),
- the domain decomposition with triangle/tetrahedron elements,
- the introduction of an artificial pressure in the structure subdomain
- and the utilization of a specific stiffness coefficient for the mesh motion problem.

The method is successfully applied and validated by comparing its results to numerically computed reference data of a benchmark setting described in [31]. For that purpose, the open-source computing platform FEniCS [3] is used.

Furthermore, an innovative method introduced in [1] for the solution of the fluid flow is incorporated into the monolithic procedure in order to allow a simpler spatial discretization with solely linear finite elements (P1P1P1). The resulting new approach for the computation of FSI is also validated with the reference data given in [30].

In a third and last step, the monolithic approach with linear elements (P1P1P1) is successfully extended to a solution method for thermomechanical FSI. The coupling and extension to the temperature is realized for an incompressible Navier–Stokes–Fourier fluid and a compressible, linear thermoelastic structure by including the balance of entropy. A qualitative evaluation of the computed results indicates the appropriateness of the developed approach for the computation of thermomechanical FSI problems.

Although applied to a simple two-dimensional benchmark setting, the developed methods can generally be utilized for arbitrary and complex applications provided that the computational time and resources do not exceed certain limits.

Nevertheless, there still exist many possibilities for the improvement and continuation of the presented work:

- The development of iterative solvers for the resulting systems of linear equations would increase the computation performance for large systems significantly. According to the author's assessment, the use of a direct solver practically restricts the developed approaches to systems with less than one million degrees of freedom.
- An automation and exclusion of the mesh motion problem from the actual FSI formulation would decrease the degrees of freedom of the linear systems drastically. An exclusion of the pressure unknown in the structure subdomain would have a similar effect.
- A validation with experimental data, for example, with the data provided by [15], would enhance the credibility of the defined procedures for the mechanical FSI problem.
- The monolithic procedure could be extended to further applications like
  - free surface and multiphase flows [33],
  - compressible fluids [38].
- Other possible extensions of FSI cover the fields of
  - turbulence modelling [25],
  - contact problems [22],
  - aeroacoustics [18].
- Research on partitioned approaches with regard to different coupling algorithms and their quantitative comparison with monolithic procedures might improve the understanding about their applicability and efficiency. The fundamental decision between partitioned and monolithic approaches becomes essentially important in the underexplored field of thermomechanical FSI—mainly, due to the enhanced coupling of the thermal and mechanical field quantities.

List of Figures

List of Tables

Bibliography

[1] Abali, B. E. “An Accurate Finite Element Method for the Numerical Solution of Isothermal and Incompressible Flow of Viscous Fluid”. In: *Fluids* 4.1 (2019), p. 5.

[2] Abali, B. E. *Computational Reality, Solving Nonlinear and Coupled Problems in Continuum Mechanics*. Vol. 55. Advanced Structured Materials. Springer, 2017.

[3] Alnæs, M., Blechta, J., Hake, J., Johansson, A., Kehlet, B., Logg, A., Richardson, C., Ring, J., Rognes, M. E., and Wells, G. N. “The FEniCS project version 1.5”. In: *Archive of Numerical Software* 3.100 (2015).

[4] Ayachit, U. *The paraview guide: a parallel visualization application*. Kitware, Inc., 2015.

[5] Babuvška, I and Rheinboldt, W. C. “Error estimates for adaptive finite element computations”. In: *SIAM Journal on Numerical Analysis* 15.4 (1978), pp. 736–754.

[6] Bazilevs, Y., Calo, V. M., Hughes, T. J., and Zhang, Y. “Isogeometric fluid–structure interaction: theory, algorithms, and computations”. In: *Computational Mechanics* 43.1 (2008), pp. 3–37.

[7] Biancolini, M. E. *RBF Morph makes ANSYS Fluent more Flexible in RIBES Clean Sky Project*. `https://www.ansys.com/blog/rbf-morph-clean-sky`. [Online; accessed 20-July-2019]. 2018.

[8] Birken, P., Gleim, T., Kuhl, D., and Meister, A. “Fast solvers for unsteady thermal fluid structure interaction”. In: *International Journal for Numerical Methods in Fluids* 79.1 (2015), pp. 16–29.

[9] Carathéodory, C. “Untersuchungen über die Grundlagen der Thermodynamik”. In: *Mathematische Annalen* 67.3 (1909), pp. 355–386.

[10] Danowski, C., Gravemeier, V., Yoshihara, L., and Wall, W. A. “A monolithic computational approach to thermo-structure interaction”. In: *International Journal for Numerical Methods in Engineering* 95.13 (2013), pp. 1053–1078.

[11] Donea, J., Huerta, A., Ponthot, J.-P., and Rodríguez-Ferran, A. "Arbitrary Lagrangian–Eulerian Methods". In: *Encyclopedia of Computational Mechanics*. American Cancer Society, 2004. Chap. 14.

[12] Du, Y. "Numerical simulation of mechanical and thermal fluid–structure interaction in labyrinth seals". PhD thesis. Technische Universität Darmstadt, 2010.

[13] Eckart, C. "The thermodynamics of irreversible processes. I. The simple fluid". In: *Physical Review* 58.3 (1940), p. 267.

[14] Gjertsen, S. "Development of a Verified and Validated Computational Framework for Fluid–Structure Interaction: Investigating Lifting Operators and Numerical Stability". MA thesis. University of Oslo, 2017.

[15] Hessenthaler, A, Gaddum, N., Holub, O, Sinkus, R, Röhrle, O, and Nordsletten, D. "Experiment for validation of fluid–structure interaction models and algorithms". In: *International Journal for Numerical Methods in Biomedical Engineering* 33.9 (2017).

[16] Hron, J. and Turek, S. "A monolithic FEM/multigrid solver for an ALE formulation of fluid–structure interaction with applications in biomechanics". In: *Fluid–Structure Interaction*. Springer, 2006, pp. 146–170.

[17] Klunker, A. *Numerische Simulation der ebenen Kanalströmung eines inkompressiblen Bingham-Fluids mit FEniCS unter Nutzung eines nichtlinearen Materialgesetzes*. `https://www.lkm.tu-berlin.de/fileadmin/fg49/AbschlussarbeiteundProjekte/simulation/Projekt_AndreKlunker_FEMA_eines_nichtlinearen_Fluids.pdf`. [Online; accessed 15-June-2019]. 2011.

[18] Kornhaas, M., Schäfer, M., and Sternel, D. C. "Efficient numerical simulation of aeroacoustics for low Mach number flows interacting with structures". In: *Computational Mechanics* 55.6 (2015), pp. 1143–1154.

[19] Küttler, U., Förster, C., and Wall, W. A. "A solution for the incompressibility dilemma in partitioned fluid–structure interaction with pure Dirichlet fluid domains". In: *Computational Mechanics* 38.4-5 (2006), pp. 417–429.

[20] Lofink, P. "Finite element analysis of an oscillating microcantilever immersed into a fluid using fluid structure interaction in an arbitrary Lagrangian Eulerian framework". `https://www.lkm.tu-berlin.de/fileadmin/fg49/AbschlussarbeiteundProjekte/simulation/Diplomarbeit_PaulLofink_FluidStructureInteraction.pdf` [Online; accessed 02-June-2019]. 2012.

[21] Manteuffel, M. *NGSolve Examples—Fluid–structure interaction*. https://ngsolve.org/showcases/ngsolve/42-fluid-structure-interaction/. [Online; accessed 12-June-2019]. 2018.

[22] Mayer, U. M., Popp, A., Gerstenberger, A., and Wall, W. A. "3D fluid–structure-contact interaction based on a combined XFEM FSI and dual mortar contact approach". In: *Computational Mechanics* 46.1 (2010), pp. 53–67.

[23] Michler, C, Van Brummelen, E., Hulshoff, S., and De Borst, R. "The relevance of conservation for stability and accuracy of numerical methods for fluid–structure interaction". In: *Computer Methods in Applied Mechanics and Engineering* 192.37-38 (2003), pp. 4195–4215.

[24] *MUMPS: MUltifrontal Massively Parallel sparse direct Solver*. http://mumps.enseeiht.fr/. [Online; accessed 06-August-2019].

[25] Pironkov, P. "Numerical simulation of thermal fluid–structure interaction". PhD thesis. Technische Universität Darmstadt, 2010.

[26] *Polypropylen Homopolymer (PP-H)*. https://www.kern.de/de/technisches-datenblatt/polypropylen-pp-h?n=1502_1. [Online; accessed 08-August-2019].

[27] Slyngstad, A. S. "Verification and Validation of a Monolithic Fluid–Structure Interaction Solver in FEniCS. A comparison of mesh lifting operators." MA thesis. University of Oslo, 2017.

[28] Stein, K., Tezduyar, T., and Benney, R. "Mesh moving techniques for fluid–structure interactions with large displacements". In: *Journal of Applied Mechanics* 70.1 (2003), pp. 58–63.

[29] Taylor, C. and Hood, P. "A numerical solution of the Navier-Stokes equations using the finite element technique". In: *Computers & Fluids* 1.1 (1973), pp. 73–100.

[30] Turek, S. *Numerical Benchmarking of Fluid–Structure Interaction between an elastic Object and laminar incompressible Flow - Reference Values*. http://www.featflow.de/en/benchmarks/cfdbenchmarking/fsi_benchmark/fsi_reference.html. [Online; accessed 16-July-2019].

[31] Turek, S. and Hron, J. "Proposal for numerical benchmarking of fluid–structure interaction between an elastic object and laminar incompressible flow". In: *Fluid–Structure Interaction*. Springer, 2006, pp. 371–385.

[32] Turek, S., Hron, J., Razzaq, M., Wobker, H., and Schäfer, M. "Numerical benchmarking of fluid–structure interaction: A comparison of different discretization and solution approaches". In: *Fluid Structure Interaction II*.

Ed. by Bungartz, H. J., Mehl, M., and Schäfer, M. Vol. 73. Lecture Notes in Computational Science and Engineering. Springer, 2011, pp. 413–424.

[33] Walhorn, E., Kölke, A., Hübner, B., and Dinkler, D. "Fluid–structure coupling within a monolithic model involving free surface flows". In: *Computers & Structures* 83.25-26 (2005), pp. 2100–2111.

[34] Wall, W. A. "Fluid–Struktur–Interaktion mit stabilisierten Finiten Elementen". PhD thesis. Universität Stuttgart, 1999.

[35] Wick, T. "Adaptive finite element simulation of fluid–structure interaction with application to heart-valve dynamics". PhD thesis. Universität Heidelberg, 2011.

[36] Wick, T. "Fluid–structure interactions using different mesh motion techniques". In: *Computers & Structures* 89.13-14 (2011), pp. 1456–1467.

[37] Yang, Z. "Analysis of lattice Boltzmann boundary conditions". PhD thesis. Universität Konstanz, 2007.

[38] Yin, L., Jiang, J.-c., and Zhang, L.-x. "Monolithic approach to thermal fluid–structure interaction with nonconforming interfaces". In: *Applied Mathematics and Mechanics* 33.2 (2012), pp. 211–222.

A Analytical solution for a laminar channel flow

In this chapter the analytical solution of a steady-state parallel flow through a channel is derived in 2D Cartesian coordinates.

Let a Cartesian coordinate system be positioned in the center of the channel as in Fig. 3.1, where $x \widehat{=} x_1$ and $y \widehat{=} x_2$, and let the body force f_i be neglected. Then the balance of mass, Eq. (3.4), and the balance of linear momentum, Eq. (3.5), for an incompressible fluid modeled by the NAVIER–STOKES's constitutive relation read

$$\frac{\partial v_1}{\partial x_1} + \frac{\partial v_2}{\partial x_2} = 0, \tag{A.1}$$

$$\rho v_1 \frac{\partial v_1}{\partial x_1} + \rho v_2 \frac{\partial v_1}{\partial x_2} = -\frac{\partial p}{\partial x_1} + \mu \left(\frac{\partial^2 v_1}{\partial x_1 \partial x_1} + \frac{\partial^2 v_1}{\partial x_2 \partial x_2} \right), \tag{A.2}$$

$$\rho v_2 \frac{\partial v_2}{\partial x_2} + \rho v_1 \frac{\partial v_2}{\partial x_1} = -\frac{\partial p}{\partial x_2} + \mu \left(\frac{\partial^2 v_2}{\partial x_2 \partial x_2} + \frac{\partial^2 v_2}{\partial x_1 \partial x_1} \right). \tag{A.3}$$

If the flow is directed towards x_1, then we assume that $v_2 = 0$. Hence, the gradients of v_2 are also equal to zero:

$$\frac{\partial v_2}{\partial x_2} = \frac{\partial v_2}{\partial x_1} = \frac{\partial^2 v_2}{\partial x_2 \partial x_2} = \frac{\partial^2 v_2}{\partial x_1 \partial x_1} = 0. \tag{A.4}$$

From Eq. (A.1) follows that

$$\frac{\partial v_1}{\partial x_1} = -\frac{\partial v_2}{\partial x_2} = 0 \Rightarrow \frac{\partial^2 v_1}{\partial x_1 \partial x_1} = 0. \tag{A.5}$$

Consequently, the balances of linear momentum in Eq. (A.2) and Eq. (A.3) reduce to

$$\frac{\partial p}{\partial x_1} = \mu \frac{\partial^2 v_1}{\partial x_2 \partial x_2}, \tag{A.6}$$

$$\frac{\partial p}{\partial x_2} = 0. \tag{A.7}$$

Assuming that the pressure is only a function of x_1, Eq. (A.6) can be integrated

twice in x_2 such that

$$v_1 = \frac{1}{2\mu}\frac{\partial p}{\partial x_1}x_2^2 + Cx_2 + D, \tag{A.8}$$

where C and D are constants. These constants are determined using the boundary conditions:

$$v_1(x_2 = -r) = v_1(x_2 = r) = 0 \Rightarrow D = -\frac{r^2}{2\mu}\frac{\partial p}{\partial x_1} \Rightarrow C = 0, \tag{A.9}$$

where r is half of the channel diameter. The obtained analytical solution reads

$$v_1 = -\frac{r^2}{2\mu}\frac{\partial p}{\partial x_1}\left(1 - \left(\frac{x_2}{r}\right)^2\right) = v_x^{HP}. \tag{A.10}$$

The analytical velocity profile described by Eq. (A.10) attains its maximum in the center of the channel at $x_2 = 0$ and reduces quadratically to zero at the channel walls at $x_2 = \pm r$. It is also known as velocity distribution of the HAGEN–POISEUILLE channel flow and therefore denoted by v_x^{HP}. Note that it is often specified in cylindrical coordinates in the literature leading to an additional factor of $\frac{1}{2}$ in Eq. (A.10).

For the channel flow problem in Sect. 3.2 the pressure gradient is constant and can hence be determined as follows:

$$\frac{\partial p}{\partial x_1} = \frac{p^{\text{out}} - p^{\text{in}}(t = t^{\text{bc}})}{l}, \tag{A.11}$$

where l is the length of the channel.